This is to certify that the
thesis entitled

WAVE ROTOR TEST RIG DESIGN PROCEDURE FOR
GAS TURBINE ENHANCEMENT

presented by

Pranav Ajit Sané

has been accepted towards fulfillment
of the requirements for the

Master of Science degree in Mechanical Engineering

Major Professor's Signature

02/5/08

Date

DATE DUE	DATE DUE	DATE DUE

WAVE ROTOR TEST RIG DESIGN PROCEDURE FOR GAS TURBINE ENHANCEMENT

By

Pranav Ajit Sané

A THESIS

Submitted to
Michigan State University
in partial fulfillment of the requirements
for the degree of

MASTER OF SCIENCE

Department of Mechanical Engineering

2008

ABSTRACT

WAVE ROTOR TEST RIG DESIGN PROCEDURE FOR GAS TURBINE ENHANCEMENT

By

Pranav Sané

Wave rotor technology has been in its development stages for close to a century now. The complexity of the wave phenomenon and the computational difficulties were some of the biggest reasons why the technology hasn't gained prominence. Recent advancements in controls, increased research in pressure waves and improved computational power has rejuvenated this fascinating technology. In the quest for improving the efficiency of power generation devices while keeping emissions low, wave rotors have a bright future. Wave rotors are essentially energy exchange devices that transfer energy between two media. This body of research is focused towards the efficient design of a viable porting to be used on a test rig for gas turbine enhancement. In the first part of this research, an algebraic code developed at MSU is described which can provide a porting geometry for any given operating condition while estimating the amount of exhaust gas recirculation. The code was benchmarked using two commercial codes, a one dimensional code GT-POWER and a two dimensional computational fluid dynamic code, FLUENT. The agreement between the codes shows the strength of the 1D algebraic code and how it can be used for the preliminary development stage. The second part of this work deals with the future developments of wave rotors and the innovative designs that can be used to improve this technology.

To My Grandfather

ACKNOWLEDEMENTS

First and foremost, I would like to thank Dr. Norbert Müller for giving me this wonderful opportunity and introducing me to the pressure wave supercharging technology. I am deeply indebted to him for helping me learn research techniques ground up. The considerable leeway he provided initially to find a foothold and then the subsequent interaction to direct my work has really helped me. He is one of the most wonderful people I have ever met and I have learnt a lot from him inside and outside our work together. I hope and pray this acquaintanceship lasts a lifetime.

I would also like to thank Mr. Luděk Pohořelský for his incredible support and stimulating conversations. He helped my knowledge curve grow exponentially and made me achieve more than I had expected from myself. His ability to keep working consistently while remaining jovial and retaining his humility is one of the most awe inspiring facets of his nature. I truly value his friendship and knowledge.

My immense gratitude to my committee members, Dr. Craig Somerton and Dr. Abraham Engeda for their support and inputs that helped me complete this thesis.

I also thank all the lab members of the Turbomachinery Laboratory for their wonderful company and the intellectual gymnasium that they all help create. Kanishka Sharma was a great companion and supporter for my research work and a lot of the CFD simulation results were achieved thanks to him. Marco Vagani was a wonderful trouble shooter and an immense help with any and everything related to the simulations we ran. Another

great supporter to our efforts was David Biegas and a majority of the test rig manufacture was completed by his skilled hands.

I would like to thank Dr André Bénard for all the fruitful discussions I have had with him about my research and the patience he has shown with me with my incessant questions.

A very big thanks to my friends Rajat, Siddharth, Arjun, Ratikant, Mitali and Krishnadev who have been as accommodating as they could during the course of my work at MSU and in the final stages during the typing of my thesis. I would also like to thank all my friends who helped cheer me in my time of sadness and celebrated with me in my happiness.

Most importantly, I would like to thank my pillars, my family. Their unconditional support and continuous encouragement has sheltered me throughout my life and theirs is a debt I cannot repay. The words of my parents and their love have helped me in this time away from home.

Finally, I dedicate this work to my late grandfather who passed away while I was working on my masters. I thank you for teaching all of us the value of character and honesty and I will always remember you for the kindness you bestowed upon your children and grandchildren.

TABLE OF CONTENTS

LIST OF TABLES

LIST OF FIGURES

Images in this thesis are presented in color

CHAPTER 1

INTRODUCTION & HISTORICAL OVERVIEW

1.1 INTRODUCTION

During the Industrial Revolution, the number of energy producing devices increased exponentially and man began abusing this new found power. Efficiency was the least of his concerns and power requirements were easily scaled with size. In this way, we continued for the next three hundred odd years without a care about the steadily depleting resources and the increasing pollution.

In the middle of the 20th century, people began addressing these issues seriously and the onus was shifted onto the new breed of designers and engineers to come up with higher efficiency devices and processes to make up for previous mistakes.

The pressure wave supercharging process was one of these discoveries.

The pressure wave exchange process deals with the energy and enthalpy exchange between two media without the use of a mechanical device such as blades or pistons. Fig. 1 shows the comparison of the isentropic efficiency of shockwaves in a frictionless channel with diffusers and compressors with respect to the pressure ratio of compression [2]. As seen, the shockwave is unmatched till a pressure ratio of 2.2 beyond which a diffuser begins to achieve better performance. A shockwave is also more efficient than a compressor up to a pressure ratio of close to 3. We must accept that accounting for

friction factors will reduce the efficiency of the shockwave but is still expected to outperform the other two. At low pressure ratios, the efficiency of the shockwave is so much higher than the other two that it is a logical choice for its application to devices which run in that operation region.

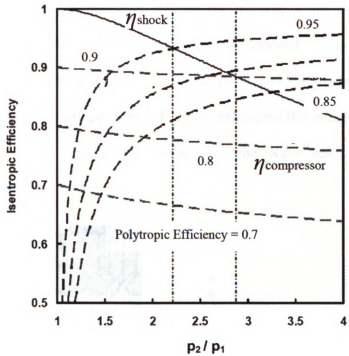

Fig. 1 Isentropic efficiency of shockwave, compressor and diffuser with respect to pressure ratio [2]

For gas turbine applications, it is essential to maximize the power output and efficiency of the cycle. Fig. 2 shows a comparison of a wave rotor topped and a baseline cycle on a Temperature - Entropy (T - s) chart. Consider a baseline cycle (subscript 'b'), air is compressed by the compressor from state 0 to 1_b. After this stage, fuel is added to the compressed air and combusted in the combustion chamber. This changes the state from 1_b to 4_b as a heat addition process. Exhaust gas at this stage enters the turbine with

temperature TIT (Turbine Inlet Temperature) where it expands to give work and changes state from 4_b to 5_b.

The wave rotor topped cycle changes the baseline cycle to 0-1-2-3-4-5. As the pressure ratio is higher for the wave rotor topped cycle, after the combustor stage it produces a much higher TIT. The TIT is normally limited by material considerations and hence the altered cycle achieves a temperature beyond the material limits of the turbine. The strategy used to decouple the high temperature of the gas exiting the combustor and the material limits of the turbine is by expanding the gas in an appropriate device which will lower the temperature to a reasonable TIT while exchanging this energy to the air coming from the compressor. This is the essence of the wave rotor enhancement for thermodynamic cycles.

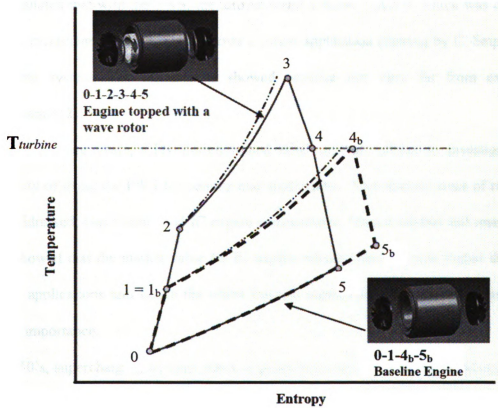

Fig. 2 T-s diagram for baseline and wave rotor topped gas turbine cycle [2]

1.2 HISTORICAL OVERVIEW

The first proposal of a pressure wave exchanger was in a patent by a German engineer, Burghard in 1913 [3]. His idea was to use a rotating drum with circular axial channels evenly spaced around the periphery of the drum which would be a continual source of pressurized air. Due to the lack of knowledge of unsteady flow theory in that period, his machine never made it to production.

The inception of the pressure wave supercharger (PWS) was around the 1940's by Swiss engineer Claude Seippel who worked at the Brown Boveri Corporation (BBC, now known as Asea Brown Boveri (ABB)). Seippel coined the term 'COMPREX' due to the **COM**Pression-**EX**pansion process that took place within the rotor channels. His first attempt was to apply the PWS to supercharge a 1640kW gas turbine locomotive engine. He calculated that with the PWS, the turbine could achieve 2983kW which was close to an 80% increment in power. Fig. 3 shows a patent application drawing by C. Seippel for the same system. The initial tests showed promise but were far from expected performance [2].

In the following years, ETH Zurich joined BBC in their efforts to investigate the feasibility of using the PWS for commercial applications. Two distinct areas of research were addressed; Gas turbine and IC engine enhancement. Market studies and research at BBC showed that the market value for IC engine enhancement [1] was higher than gas turbine applications and hence the effort towards supercharging of engines was given greater importance.

In the 50's, supercharging of truck diesel engines was taken up with the collaboration of ETH Zurich, ITE Circuit Breaker Company and BBC. Cornell University also joined in

to aid ITE during the development stages for these diesel engines. Power Jets Ltd in the UK started working on multiple wave rotor applications around the same time. Though Power Jets' initial intent was to use the wave rotor for IC engine supercharging, they investigated other applications like gas turbines, pressure equalizers, dividers and air cycle refrigeration units. After the death of the founder, the work was continued at the Imperial College and University of London and at the Ricardo Company.

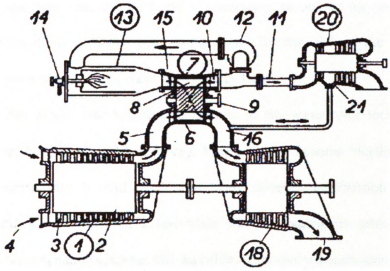

Fig. 3 A gas turbine topped wave rotor [From Ref. 11]

In the mid 50's, a new kind of wave rotor design called the Pearson Rotor was designed at the Ruston-Hornsby Turbine Company in the UK. This was known as the wave turbine engine as it used helical channels to produce shaft work the same way a gas turbine would. The company unfortunately ran into financial trouble and Pearson was unable to find a funding agency for his device. Due to the apparent financial difficulties, research on the Pearson Rotor ended beyond that point.

In the 70's, the COMPREX® was tested by Mercedes-Benz for the supercharging of their passenger diesel engines. Around the same time, a Finnish company called Valmet

applied the COMPREX® to their line of tractor engines. In 1979, BBC also tested a racing version of the COMPREX® for F1 cars but it never made it to production.

In the 1980's, a number of automobile manufacturers began taking interest in the COMPREX® and was tested by Mazda, Peugeot, Opel, Mercedes-Benz and Ferrari. The one's that went into mass production were the 2.3 litre supercharged engines on the Opel Senator [23] and the 2.0 litre supercharged engine on the Mazda 626 Capella. The Capella sold more than 150,000 units and is considered as one of the most successful commercial applications of wave rotor technology. By the end of the 1980's ABB transferred the wave rotor development to Mazda in Japan.

Some of the other places that had looked intently at the wave rotor technology were General Electric, NASA, ONERA (France), Mathematical Science Northwest Inc. and the Naval Postgraduate School. GE tested an internal combustion wave rotor configuration but gave it up after a few trials which revealed the problems with its mechanical and aerodynamic systems. GE was able to achieve pressure gains between 1.2 and 1.3 at their test rigs but expansion of the rotor, leakages and failure at the tests led to the closing of the research program.

Scientists at NASA's Glenn Research Center worked on a number of numerical models for wave rotors and also tested a four port wave rotor (Fig. 4) but cancelled their program after the rotor seized at the test rig. Paxson performed feasibility studies for engines topped with wave rotors and he also developed a 1D gas dynamic code for analyzing wave rotor performance. Rolls-Royce Allison and Swissauto Engineering are some of the few companies presently pursuing research on wave rotors.

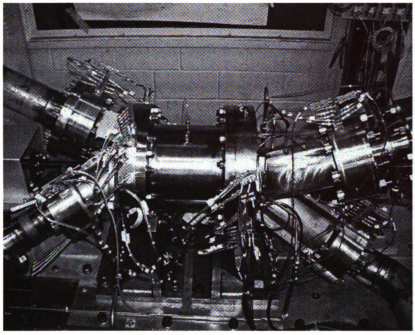

Fig. 4 Four Port Wave Rotor test Rig at NASA [2]

Recently a number of universities (ETH Zurich, Warsaw University, Michigan State University, Indiana University Purdue University Indianapolis, University of Tokyo and Beijing University of Technology) have been working on the development of various aspects of wave rotor technologies.

Presently the development work on IC engine supercharging at ETH Zurich (Guzzella et al) is being pursued in close collaboration with Swissauto WENKO and have been focusing on the control issues for the pressure wave superchargers. Piechna at Warsaw University has proposed the development of a wave rotor with internal combustion and presently considerable analysis work is being pursued in development of internal combustion wave disc engines.

The development of wave rotor technology over the years in its many application fields has been summarized by Akbari [2] in Fig. 5.

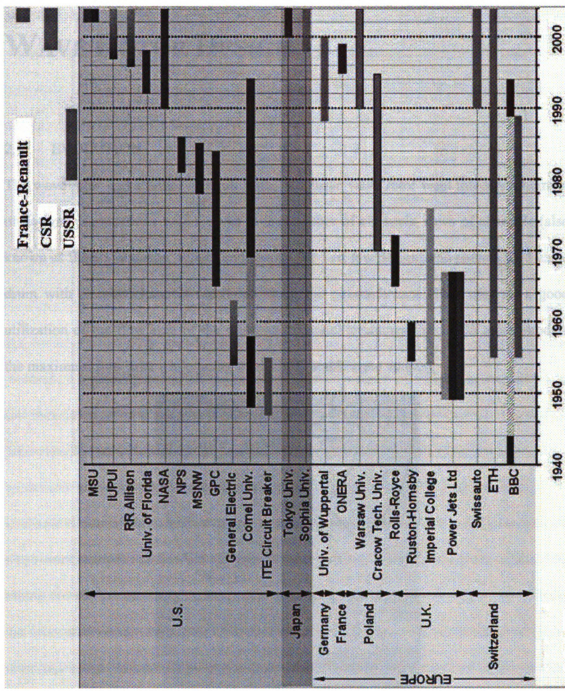

Fig. 5 Chronological description of progress on wave rotor technologies [2] (Red: Gas Turbine Application; Green : IC Engine Supercharging ; Blue : Refrigeration Cycle ; Pink : Pressure Divider and Equalizer ; Purple : Wave Superheater ; Orange : Internal Combustion Wave Rotors ; Black: General Applications)

CHAPTER 2

WAVE ROTOR DESIGN

2.1 EVOLUTION

The wave rotor had a rather difficult birth. The basic wave rotor went through a number of designs permutations with respect to the number of channels, rows of channels (also known as flutes), diameter, length and shape. The first few designs and patents filed had a drum with circular channels machined along the circumference. This was not a good utilization of the flow area of the drum and channel structures that could accommodate the maximum flow area while being structurally stable were studied.

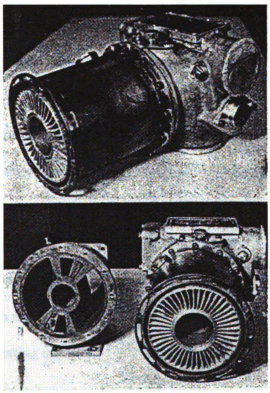

Fig. 6 The COMPREX® from the 1960's [4]

As a design constraint the number of channels had considerable conflicting parameters. If the number of channels increase, there is a higher probability of achieving a one dimensional flow but this increases the entry flow losses and reduces the maximum utilization of flow area of the rotor. A compromise had to be met for the final design to accommodate all of these factors.

The next challenge that Brown Boveri & Cie (BBC) had to deal with was the material constraints for such an application [14]. Due to high rotor speeds, the material would have to handle large centrifugal forces and a high excitation frequency which was close to the 20^{th} order of the fundamental frequency and sometimes higher due to the shockwaves. In addition, the material had to be able to withstand the thermal stress due to the cyclic temperature gradients of the operation. Through many years of material research, a new alloy based on Invar (an alloy of iron and nickel) was chosen due to its low thermal expansion, high corrosion resistance, ductility and high strength. All of these properties had to be achieved without using exotic alloying materials which could drive up the cost of production.

Leakage is one of the most important factors that affects the performance of pressure wave machines and for the same reason, it was decided that the rotor and the mantle (the casing around the rotor) would have to be of the same low expansion material. Finally, the alloy that met all of these conditions was used by BBC to mass produce the wave rotor and is known commercially as BBC 243. It was tested extensive for its thermal and mechanical properties in tests such as the 'burst-test' (Fig. 7). The burst test is a common testing procedure for rotating machinery in which a component is spun with an increasing speed till it fails due to the centrifugal forces or imbalance.

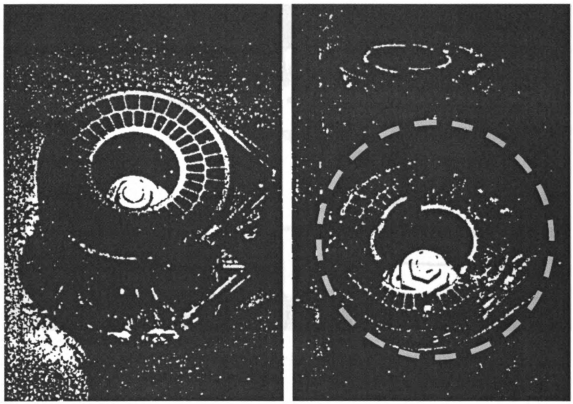

Fig. 7 Burst test conducted on a wave rotor [15]

The next task was to achieve the ability to manufacture this kind of a rotor on a large scale. The process chosen for such a complex part was precision investment casting due to the complexity of the structure and the high requirement for process control. The alloy had to be cast under vacuum in an induction furnace (Fig. 8) to generate the rotor which then had its faces and hub machined by fine grinding and then made ready for assembly. Over a period of time the main stages of the production process were automated and were able to achieve extruded wall thicknesses down to 0.5mm with a good surface finish. It took ABB close to five years to hone the manufacturing process to mass produce the COMPREX® wave rotor.

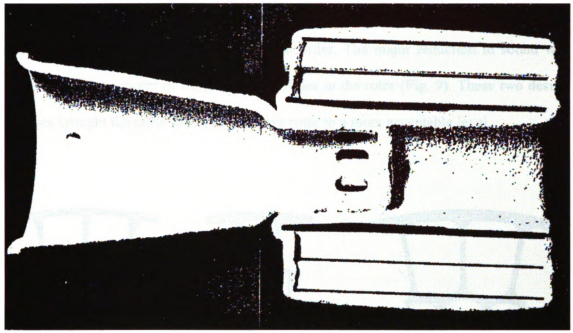

Fig. 8 Ceramic mould used to manufacture the rotor by precision casting [14]

When the wave rotor was put to the test, due to the symmetry of the cells, a high pitch 'whistle' [27] was generated during its operation which was extremely disagreeable. The frequency of this 'whistle' is given by

$$f = \frac{i z n}{60} \tag{1}$$

Where,

i whole number

z number of rotor channels ($z > 1$)

n rpm of rotor

For a rotor spinning between 2500 rpm and 15000 rpm, the fundamental frequency of the noise lies between 1400 and 8500 Hz (assuming a 34 channel rotor). This frequency range lies in the audible zone and would be necessary to eliminate as the human ear is sensitive to this frequency band.

The problem of the sound was dealt with by breaking the symmetry of the cells by using cells of different areas arranged in a broken order. The major reduction in sound was achieved by the concept of using multiples flutes in the rotor (Fig. 9). These two design changes brought the noise levels of the wave rotor to a more acceptable level.

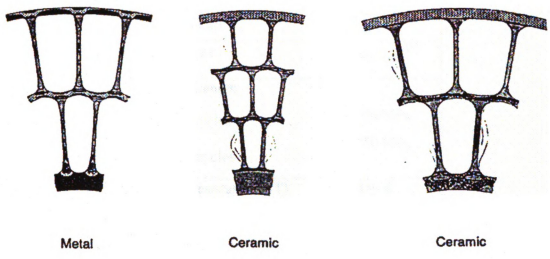

Fig. 9 Different wave rotor flutes designed as per material used [15]

After the processes for mass production of the wave rotor and other nagging issues such as the noise emissions had been solved, ABB decided to foray into the world of ceramic materials to design the wave rotors. ABB worked closely with NGK Insulators Ltd to find appropriate ceramic materials due to the history and expertise that NGK Insulators had with ceramics. They tested an alloy called Ni Co Ti 43 2 2 Nb and also Silicon Nitride (Si_3N_4) as ceramics were considerably lighter, stronger and had lower thermal expansion coefficients. The material finally tested by ABB was a pressure-less sintered silicon nitride designated SN-75 (Table 1).

Property	Value
Density	3200 kg/m^3
Bending Strength 20 °C 800 °C	 470 MPa 440 MPa
Modulus of elasticity	275 GPa
Poisson's ratio at 20 °C	0.27
Fracture toughness	5.9 MN/ m$^{3/2}$
Cyclic fatigue strength 20 °C and 10^8 cycles 800 °C and 10^8 cycles	 > 250 MPa > 250 MPa
Thermal shock resistance (ΔT)	550 K
Thermal conductivity	30 W/mK
Thermal expansion coefficient (40 – 600 °C)	3.1×10^{-6} /K
Resistance to oxidation Weight gain 1000h at 750 °C	< 0.1 mg/ cm^2

Table 1 Properties of extruded SN-75 [15]

As the traditional wave rotor was made of metal and was heavy, it was difficult to operate in a 'free running' condition [29]. Due to its high inertia it had to be belt driven from the crankshaft to be able to respond immediately to the varying load conditions. Using ceramic materials would make to rotor capable of free running and would thus consequently reduce the parasitic load on the crankshaft while being able to respond immediately to throttle position or load condition.

The COMPREX® has a designation CX followed by a number which is used to denote the diameter and length. Most wave rotors produced by ABB had a length/diameter ratio of 1. The CX series had been designed for a wide range of engine output values (Table 2). For example, the CX-93 was used on a Mazda 626 engine and the CX-64 is being used on the Greenpeace sponsored SmILE car.

For passenger car application			
Designation	Range of engine output (supercharged) (kW)	Rated Speed (RPM)	Weight (total) kg
CX 112	60 – 100	15200	11.6
CX 102	50 – 83	16700	8.4
CX 93	40 – 70	18300	7.2
CX 85	35 – 57	20000	6.2
CX 78	30 – 48	21800	5.4
CX 71	25 – 40	23900	4.9

Table 2 COMPREX® model line for passenger car applications [From ref. 22]

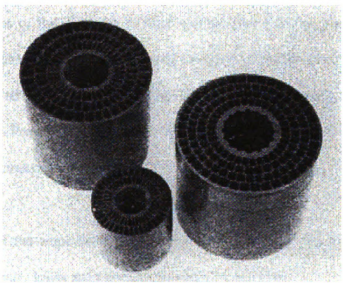

Fig. 10 Wave rotors designed over the years with changing material and design [17]

The rotor studied at MSU was the CX-93 which was taken from a Mazda 626 Capella 2.0 litre diesel engine.

2.2 FLOW CONFIGURATIONS

The wave rotor can be operated in two flow configurations, namely (a) through-flow and (b) reverse-flow. The flow configurations are explained below using a space-time diagram. The horizontal axis for the flow configuration diagrams is the rotor axial length while the vertical axis is time. The rotor channels are shown in a developed view and rotate from the bottom to the top.

For both the diagrams of the flow configurations, the red dashed box denotes the high pressure (HP) region while the blue dashed box denotes the low pressure (LP) region.

2.2.1 THROUGH FLOW CONFIGURATION

For the through-flow configuration (Fig. 11) each end plate handles both fluids and hence is divided in terms of the direction of flow motion. One side can be considered as the inlet side as it houses both Air and Exhaust Gas inlets while the other can be considered the outlet side. In terms of pressure zones the channels can divide into two regions which comprise the High Pressure (HP) and Low Pressure (LP) region which can further be sub-divided into ten states or zones, namely,

1- The zone of the rotor filled with air or a mixture from the previous cycle at a pressure slightly lower than ambient because of the inflow.

II - This zone is created by the first shockwave (S1) which propagates due to the large pressure at the EI port and travels towards the AO port.

III - This zone is created by the second shockwave (S2) which increases the pressure of zone *III* and propagates from the AO port to the EI port

IV - This zone is created by the first expansion wave (E1). This zone separates the HP region from the LP region after the first expansion wave, E1. The air-gas components of the zone expand to the zone pressure due to E1.

V - This zone is created by the second expansion wave (E2) which is created by the sudden opening of zone *IV* to the EO port. E2 propagates as a strong expansion wave in the low pressure region from the EO port towards the AI port.

VI - This zone is created by the third expansion wave (E3). E2 rebounds at the AI port and propagates towards the EO port as a weak expansion wave.

VII - This zone is created by the first pressure wave (P1). As the returning wave E3 opens directly into the EO port, it returns as a weak pressure wave P1.

VIII - This zone is created by the fourth expansion wave (E4). As the AI port is still open, P1 is reflected as E4 and propagates from the AI port to the EO port

IX - This zone is created by the second pressure wave (P2) which travels from the EO port to the AI port due to similar interactions as before. Pressure and expansion waves in the low pressure part are weak.

X - This zone is created by the fifth expansion wave (E5). The mixture of fresh air and exhaust gas expands through E5 to reach the same condition as the beginning of the cycle. If any EGR is present from the previous cycle, it is exhausted to the AO port.

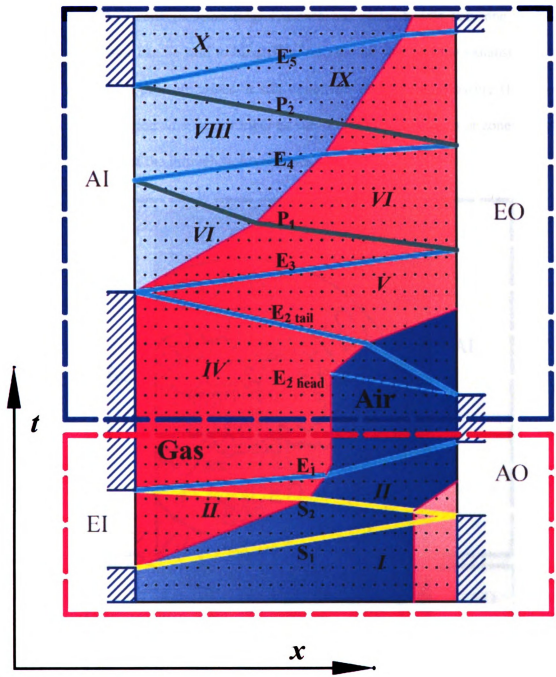

Fig. 11 Through Flow Configuration

2.2.2 REVERSE FLOW CONFIGURATION

For the **reverse-flow configuration** (Fig. 12) each end plates handle only one kind of fluid. Hence the rotor can be said to be divided into the air side and the exhaust side at each end. In terms of pressure zones, it still comprises of the High Pressure (HP) and Low Pressure (LP) region which can further be sub-divided into ten states or zones which match the conditions of the through flow configuration.

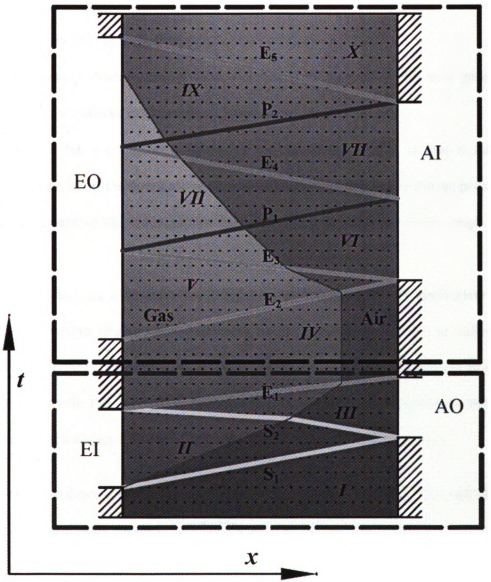

Fig. 12 Reverse Flow Configuration

Though the reverse flow configuration has been used more extensively in the industry, the through flow configuration has the benefit of better temperature distribution. For the reverse flow, the exhaust side remains very hot and creates a problem for the bearings.

2.3 COMMERCIAL APPLICATION

A few automotive companies that tried to implement the wave rotor technology to supercharge their engines are Mazda, Peugeot, Opel, Mercedes-Benz, Volkswagen, Ferrari and Renault [18], [19], [23].

A Swiss company, Swissauto WENKO AG has been pioneering the next generation COMPREX® for gasoline engines which is known as the HYPREX®.

An issue with the wave process for either of the configurations is that it tends to deteriorate very fast if the boundary conditions change from the perfect tuning point. This makes the control of the wave pattern hard and also limits the operation range of the device.

Swissauto worked on a reverse flow configured wave rotor for its application to an internal combustion engine and is shown in Fig. 13. They utilize the so called 'gas pockets' to account for the mass flow variation within the rotor with respect to engine speed and provide the supercharger the ability to adapt to the variation in boundary conditions which allows it to perform well at a wide range of load conditions.

The pockets are depressions in the air and exhaust side end plates which through changes in boundary conditions generate new pressure waves that alter the previous wave pattern. These enable the control of the pressure wave process over a wide speed and load range. There are 2 pockets per cycle on the air side; the compression pocket (CP) (Fig. 14)

which corrects the wave pattern at low speeds/low loads and the expansion pocket (EP) which maintains sufficient scavenging over the entire operating range in interaction with the gas pocket (GP) on the gas side (Fig. 15).

The design of the pockets has helped aid the transient response of the pressure wave supercharger while extending the operation range of the engine [6].

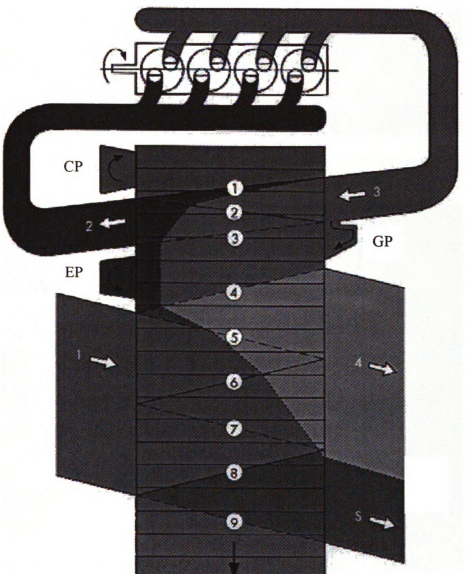

Fig. 13 Porting geometry scheme with pockets by Swissauto WENKO AG

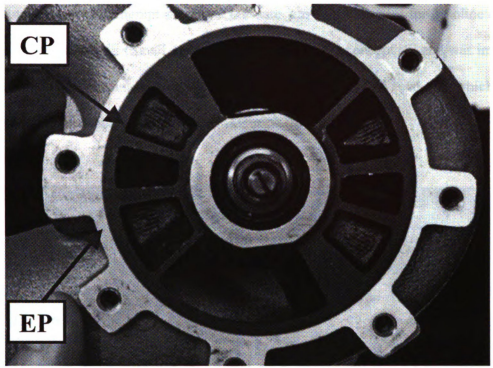

Fig. 14 Air side with the Compression Pocket (CP) and Expansion Pocket (EP) for the CX-93

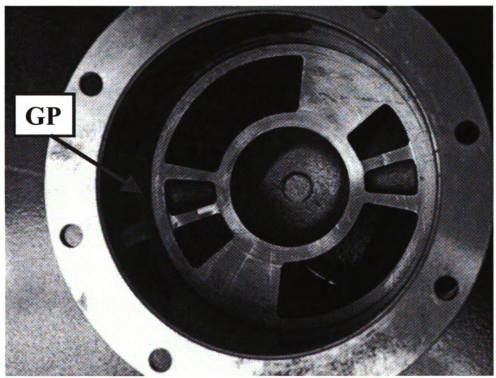

Fig. 15 Exhaust side with ports and Gas Pocket (GP) for the CX-93

Swissauto's successful attempt at using a pressure wave supercharger for gasoline engine has been with the SAVE (Small Advanced Vehicle Engine) concept [5] and was installed into the **SmILE** (**Sm**all-**I**ntelligent-**L**ight-**E**fficient) (Fig. 16) project which was completed in close collaboration with ETH Zurich for Greenpeace.

Fig. 16 The SmILE car (Left) and a view of the Engine with the HYPREX (Right)

The SmILE car is effectively a Renault Twingo which has an altered drivetrain and improved aerodynamics. The powerplant is a 360cc boxer engine boosted with a HYPREX® supercharger which is targeting a 25% reduction in fuel consumption compared to a naturally aspirated engine of equal power.

CHAPTER 3

ONE DIMENSIONAL WAVE DYNAMIC CODE

3.1 INTRODUCTION

Due to the demanding task of generating a viable porting geometry for a pressure wave supercharging device like the wave rotor, a one dimensional code was developed at the Turbomachinery Laboratory at Michigan State University to algebraically code the wave interactions and provide the output of a porting geometry and its operation speed. A fixed number of wave interactions were considered by reviewing previous work on pressure wave superchargers and a flow configuration of two shockwaves and one expansion wave was assumed to define the high pressure region. For the low pressure region, 6 wave interactions were selected. 4 expansion waves and 2 pressure waves. The reason for selecting 6 wave interactions was to allow enough time for scavenging the channels to avoid exhaust gas recirculation and also to bring the end state of the process closest to the initial state. For a through-flow configuration as described below, in the low pressure region, the pressure and expansion waves have a tendency to decrease the incidence angle (Fig. 17) of the air-gas interface after each interaction. As $\alpha_2 < \alpha_1$, every subsequent interaction would increase the retention of exhaust gas in the channels. This led to the selection of 6 interactions in the low pressure region.

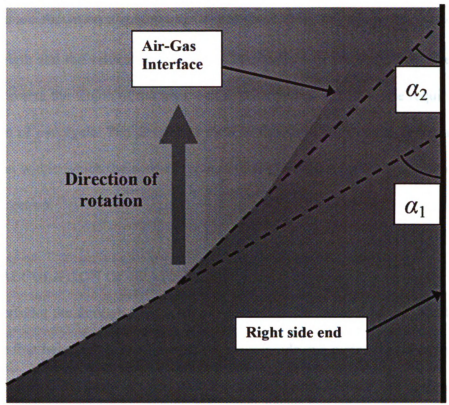

Fig. 17 Incidence Angle of Interface

3.2 ASSUMPTIONS

The code was formulated with a few assumptions to aid computation speed, decrease the complexity or neglect factors that do not play a significant role.

- The port entries are considered parallel to the rotor axis
- Flow is isentropic and there is no heat transfer from the walls
- There is no leakage between the end plates and the rotor
- Boundary layer effects are neglected
- The code was designed for a two cycle wave rotor hence the results from the code are for 180° of the rotor, i.e., half of the rotor.

The waves are shown on a space-time $(x-t)$ graph (Fig. 11) where the horizontal axis is rotor length and the vertical axis is time. The time here is the computed time for each wave to traverse the length of the rotor and hence gives us the total time required for the completion of one cycle. The developed view of the wave rotor channels constitutes the flow region within which the waves propagate and the rotation of the wave rotor is in the upward direction.

3.3 CALCULATION OF STATES

We can consider the through-flow configuration to be divided as three physically distinct areas. The first being the inlet side which is the left side end plate which houses both the Air Inlet (AI) and Exhaust Inlet (EI) port, the second being the right side end plate which houses the Air Outlet (AO) and Exhaust Outlet (EO) ports. The third area is the space between the two end plates which is the developed view of the channels.

The channels before the opening of the Exhaust Inlet port are considered to be at a lower pressure than ambient due to the inflow of atmospheric air and the channels are assumed to be completely filled with air. This was defined previously as Zone *I*.

We begin the cycle at the Exhaust Inlet (EI) port, due to the pressure difference between the channels and the port, shockwave S1 is created and begins to propagate along the channel length towards the Air Outlet (AO) port.

Now, the flow velocities are different for different media. The temperature of a medium can drastically affect the wave speed and hence it is important to account for when the wave is traveling in air and in gas. Since both media are at the same pressure, the only way to distinguish them is by the temperature difference (Clarified in Chapter 4, Fig. 28).

The local speed of sound a is given by the relation,

$$a = \sqrt{\gamma RT} \tag{2}$$

Where,

R gas constant

T temperature of fluid

γ ratio of specific heat

(γ_{air} = 1.4 for air and γ_{gas} = 1.32 for exhaust gas)

HIGH PRESSURE REGION

Zone I

The channels filled with air at ambient temperature conditions make up this zone. Zone *I* can also have some exhaust gas from the previous cycle if the rotor was not fully scavenged. Zone *I* is the state of the fluid right before the opening of the Exhaust Inlet port.

Zone II

The first shockwave (S1) is considered to travel only in air as wave velocities are higher than induced flow velocities. Using shockwave relations [24], we can calculate the induced flow velocity for Zone *II*.

Let us consider the pressure ratio between the EI and the channels to be $\pi_1 = \frac{P_3}{P_{channel}}$.

Due to this compression, there is an increase in the temperature which affects the local speed of sound in that medium. The temperature increase is given by equation (3)

$$\frac{T_{II}}{T_I} = \pi_1 \left(\frac{\left(\frac{\gamma_{air}+1}{\gamma_{air}-1} \right) + \pi_1}{1 + \left(\frac{\gamma_{air}+1}{\gamma_{air}-1} \right) \pi_1} \right) \tag{3}$$

Here T_{II} and T_I are the temperatures of the respective zones.

The resulting wave speed w_{S1} is given by the equation,

$$w_{S1} = a \sqrt{1 + \left(\frac{(\gamma_{air}+1)(\pi_1 - 1)}{2\,\gamma_{air}} \right)} \tag{4}$$

And the induced flow velocity u_{II} is given by the equation,

$$u_{II} = \frac{a}{\gamma_{air}} (\pi_1 - 1) \sqrt{\frac{2\gamma_{air} / (\gamma_{air}+1)}{\pi_1 + \left((\gamma_{air}-1) / (\gamma_{air}+1) \right)}} \tag{5}$$

In this manner, we can calculate the induced entry flow velocity of exhaust gas from the Exhaust Inlet port.

Zone *III*

To achieve a higher compression, we time the Air Outlet (AO) port opening in such a way that we allow S1 to rebound on the AO boundary. S1 reverses its direction and travels back towards the EI port as a second shockwave (S2) compressing the fluid in zone *III*.

We have already calculated the temperature increase for the air in zone *II* (T_{II}) and this lets us calculate the local speed of sound for zone *III* in air as the compressed air has an elevated temperature and hence higher local speed of sound.

$$a_{S2\_air} = \sqrt{\gamma_{air} R T_{II}} \tag{6}$$

Also, the pressure ratio for S2 changes to $\pi_2 = \frac{P_2}{P_3}$

S2 will travel through both media as the wave travels in the negative direction while the flow continues in the positive direction. For the same reason, we need to account for the variation in wave speed which will change the induced flow velocities in that respective region/zone.

$$w_{S2\_air} = -a_{S2\_air}\sqrt{1+\left(\frac{(\gamma_{air}+1)(\pi_2-1)}{2\gamma_{air}}\right)} + u_{II} \tag{7}$$

$$w_{S2\_gas} = -a_{S2\_gas}\sqrt{1+\left(\frac{(\gamma_{gas}+1)(\pi_2-1)}{2\gamma_{gas}}\right)} + u_{II} \tag{8}$$

Let us consider the movement of the air-gas interface with respect to the induced flow velocities. As the wave speeds are against the flow, they will reduce the induced flow velocity for Zone *III*. ($u_{II} > u_{III}$)

Also, the induced flow velocities in gas and air are given by

$$u_{III\_air} = u_{II} - \left(\frac{a_{S2\_air}}{\gamma_{air}}(\pi_2-1)\sqrt{\frac{2\gamma_{air}/(\gamma_{air}+1)}{\pi_2+\left((\gamma_{air}-1)/(\gamma_{air}+1)\right)}}\right) \tag{9}$$

$$u_{III\_gas} = u_{II} - \left(\frac{a_{S2\_gas}}{\gamma_{gas}} (\pi_2 - 1) \sqrt{\frac{2\gamma_{gas} / (\gamma_{gas} + 1)}{\pi_2 + \left((\gamma_{gas} - 1) / (\gamma_{gas} + 1) \right)}} \right) \quad (10)$$

And,

$$u_{III} = \frac{u_{III\_air} + u_{III\_gas}}{2} \quad (11)$$

This gives us the fluid flow velocity for Zone *III* which is the flow velocity at the Air Outlet (AO). This is one of the critical parameters for the design and it is essential to get the maximum flow rate from the AO port with the minimum amount of EGR.

When S2 reaches the EI port, due to the EI boundary condition, it reverses its direction and travels in the positive direction as an Expansion Wave (E1). As the pressure ratio is high in this region, the expansion wave is strong and hence we consider both, the head and tail of the expansion wave [A.2]. As the pressure ratio reduces, the average of the velocities of the head and tail waves makes for a good approximation.

Zone *IV*

As E1 changes the state from *III* to *IV*, *IV* is a static zone as it is closed off on both ends by the end plates and hence is a zero velocity zone $(u_{IV} = 0)$. This means that the influence of E1 is to bring state *III* to *IV*. In reality, there would still be some wave dynamics present in zone *IV* which are observed in the FLUENT simulations (Fig. 48) but are not accounted for in the 1D Algebraic code.

For the head of E1, the temperature is given by

$$\frac{T_{III\_gas}}{T_{II}} = \pi_2 \left(\frac{\left(\frac{\gamma_{gas}+1}{\gamma_{gas}-1} \right) + \pi_2}{1 + \left(\frac{\gamma_{gas}+1}{\gamma_{gas}-1} \right) \pi_2} \right) \tag{12}$$

$$\frac{T_{III\_air}}{T_{II}} = \pi_2 \left(\frac{\left(\frac{\gamma_{air}+1}{\gamma_{air}-1} \right) + \pi_2}{1 + \left(\frac{\gamma_{air}+1}{\gamma_{air}-1} \right) \pi_2} \right) \tag{13}$$

$$a_{E1\_gas} = \sqrt{\gamma_{gas} R T_{III\_gas}} \tag{14}$$

$$a_{E1\_air} = \sqrt{\gamma_{air} R T_{III\_air}} \tag{15}$$

Hence the calculated wave speeds are

$$w_{E1\_gas} = a_{E1\_gas} + u_{III} \tag{16}$$

$$w_{E1\_air} = a_{E1\_air} + u_{III} \tag{17}$$

The wave speeds help us calculate the position of the air-gas interface with respect to that wave and consequently its position along the channel length. We use the head of expansion wave E1 to define the AO closing time. The rationale behind choosing the head of the expansion wave to define the closing of a port is because when an expansion wave reaches an open space, the pressure equalization process causes the wave to return as a pressure wave which would lead to slowing down the flow at the exit of the port which is undesirable.

Another factor considered with respect to the air-gas interface in this region is that as the fluid flow velocity for the zone is zero, the interface does not change its position.

Zone *IV* is the zone that separates the high pressure region from the low pressure region. In previous work, the tail of E1 was considered to define the Exhaust Outlet (EO) opening but it has been observed that the difference between the head and tail waves is too small (≈ 20 µsec) which leaves a very small space between the AO and EO port. This would make control extremely difficult and would also be difficult to manufacture.

For the same reason, a set of 'virtual' waves were assumed to propagate (shown in black in the algebraic code output (Fig. 21)), in zone *IV*, 2 waves were calculated using pressure wave relations to propagate from the AO closing to the EO opening. This provided reasonable results without a large change in the pressure wave supercharger's tuned speed and easing the manufacturing process for the end plate geometries. The calculations for the virtual waves were done by using the following relations

$$\frac{T_{IV\_air}}{T_{III\_air}} = \left(\frac{P_{IV\_air}}{T_{III\_air}}\right)^{\frac{\gamma_{air}-1}{\gamma_{air}}} \tag{18}$$

$$\frac{T_{IV\_gas}}{T_{III\_gas}} = \left(\frac{P_{IV\_gas}}{T_{III\_gas}}\right)^{\frac{\gamma_{gas}-1}{\gamma_{gas}}} \tag{19}$$

And

$$a_{virtual\ wave\_gas} = \sqrt{\gamma_{gas}\, R\, T_{IV\_gas}} \tag{20}$$

$$a_{virtual\ wave\_air} = \sqrt{\gamma_{air}\, R\, T_{IV\_air}} \tag{21}$$

(*Note : The virtual waves have only been considered for convenience and the actual time for opening is invariant of waves. An arbitrary distance can be assumed between the AO closing and the EO opening as long as an equal sector is added to the opposite side. Having too large an arbitrary sector in Zone IV would drastically limit the porting sizes and increase the computed rotor speed as the entire wave process would have lesser time for its completion. An increase in rotor speed is again an important parameter as the motor on the test rig should be able to handle those speeds.*)

As Zone *IV* is a static zone, $u_{IV} = 0$ and hence the wave speed of the virtual wave is equal to the local speed of sound ((21) and (22)).

LOW PRESSURE REGION

All the waves that are generated in the low pressure region (except E2) propagate between a low pressure ratio and form expansion or pressure waves. The ratio is not high enough to generate shockwaves [16].

Also, due to the low pressure ratio, each wave was defined by the average velocity of its head and tail components. To compute the fluid flow velocities in the low pressure region, a technique known as the 'method of characteristics' was employed which is described in Chapter 4.

Zone *V*

The region of low pressure begins after zone *IV*. In this region, as both ends are closed, it behaves akin to a pressurized cylinder with a pressure higher than P3 ($P_{IV} > P3$). As zone *V* begins with the opening of the Exhaust Outlet port, due to the high pressure in

zone *IV*, a strong expansion wave E2 is generated at EO opening and travels towards the inlet side. As the tail of an expansion wave creates the largest pressure difference, the porting is timed in such a way that the tail of the expansion wave reaches the inlet side just as the Air Inlet (AI) port opens.

The temperature for the gas and air mass are given by equations (22) and (23).

$$\frac{T_{V\_air}}{T_{IV\_air}} = \left(\frac{P_V}{P_{IV}}\right)^{\frac{\gamma_{air}-1}{\gamma_{air}}} \tag{22}$$

$$\frac{T_{V\_gas}}{T_{IV\_gas}} = \left(\frac{P_V}{P_{IV}}\right)^{\frac{\gamma_{gas}-1}{\gamma_{gas}}} \tag{23}$$

$$a_{E2\_air} = \sqrt{\gamma_{air} R T_{V\_air}} \tag{24}$$

$$a_{E2\_gas} = \sqrt{\gamma_{gas} R T_{V\_gas}} \tag{25}$$

$$a_{E2} = \frac{a_{E2\_air} + a_{E2\_gas}}{2} \tag{26}$$

Using the method of characteristics, the induced fluid flow velocity u_V is computed by solving the equations

$$\frac{u_{V\_gas}}{a_0} = \frac{2}{\gamma_{gas}-1} \times \gamma_{gas} \times \left[\left(\frac{P_{IV}}{P_0}\right)^{\frac{\gamma_{gas}-1}{2\gamma_{gas}}} - \left(\frac{P_V}{P_0}\right)^{\frac{\gamma_{gas}-1}{2\gamma_{gas}}}\right] \tag{27}$$

$$\frac{u_{V\_air}}{a_0} = \frac{2}{\gamma_{air}-1} \times \gamma_{air} \times \left[\left(\frac{P_{IV}}{P_0}\right)^{\frac{\gamma_{air}-1}{2\gamma_{air}}} - \left(\frac{P_V}{P_0}\right)^{\frac{\gamma_{air}-1}{2\gamma_{air}}}\right] \tag{28}$$

$$u_V = \frac{u_{V\_air} + u_{V\_gas}}{2} \tag{29}$$

As E2 propagates in the negative direction, the wave speed is given as

$$w_{E2} = -a_{E2} + u_V \tag{30}$$

Zone VI

As the wave E2 arrives just before AI opening, the pressure equalization process causes E2 to return towards the right side (exhaust side) end as Expansion Wave E3. This changes the state from zone *V* to zone *VI*.

All pressure, temperature and velocity conditions are computed in a similar fashion to the Zone *V*. Following the conventions, the wave speed for E3 is given

$$w_{E3} = a_{E3} + u_{VI} \tag{31}$$

All of the subsequent zones/states can be calculated from the characteristic diagram using similar relations as above as the LP region is composed entirely of pressure and expansion waves.

Zone VII

After the expansion wave E3 reaches the EO port, it returns as a pressure wave P1 which increases the pressure of the fluid as it traverses the length of the channels while slowing down the flow as P1 propagates against the induced flow velocity.

The wave speed for P2 is given by

$$w_{P1} = -a_{P1} + u_{VII} \tag{32}$$

Zone VIII

When P2 reaches the AI port, the equalization causes it to return as expansion wave E4. As E4 propagates towards the EO port, it slows down the flow from u_{VII} to u_{VIII}. E4 changes the state in the low pressure region from zone VII to zone VIII.

The wave speed of E4 is given by equation

$$w_{E4} = a_{E4} + u_{VII} \tag{33}$$

Zone IX

After E4 reaches the EO port, it reverses and propagates in the negative direction (i.e., towards the intake side) as Pressure Wave P2. P2 travels against the flow velocity and thus slows it down.

This progressive slowing down of the flow after every wave interaction was the reason for the selection of 6 waves in the low pressure region.

The wave speed of pressure wave P2 is given by equation

$$w_{P2} = -a_{P2} + u_{VIII} \tag{34}$$

Zone X

Zone *X* is created by the expansion wave E5 which propagates after the closing of the AI port and is used to define to closing of the EO port. It is expected that E5 should be able to return the channel to the same state as zone *I* which is a static zone so that the cycle can repeat to form a steady wave pattern. As the induced fluid flow velocity should be zero, rather than forcing a zero value, a 'virtual' induced flow velocity is computed using the equation

$$\frac{u_X}{a_0} = \frac{2}{\gamma - 1} \times \gamma \times \left[\left(\frac{P_{IX}}{P_0} \right)^{\frac{\gamma - 1}{2\gamma}} - \left(\frac{P_X}{P_0} \right)^{\frac{\gamma - 1}{2\gamma}} \right] \tag{35}$$

where γ is computed for the respective fluid and the average velocity of u_X is computed. The operating conditions were filtered for low values of u_X and only values below 5 m/s were used to define operating points.

3.4 CALCULATION OF MASS FLOW RATE

For a fixed porting geometry, (Fig. 18) the flow rate at each entry or exit port is calculated by the relation (36). Mass flow rate Q is given by

$$Q = \rho A v \tag{36}$$

ρ Density of medium

A Port Opening Area

v Flow Velocity

Where

$$A = \frac{\theta}{2}\left(R_{outer}^2 - R_{inner}^2\right) \tag{37}$$

and from ideal gas equations, we have $\rho = \frac{P}{RT}$ (38)

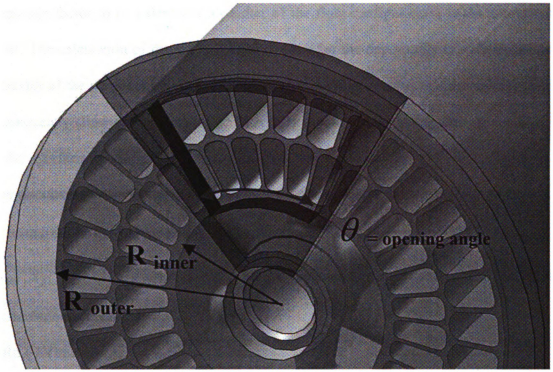

Fig. 18 Important dimensions for calculation of mass flow rate

3.5 CALCULATION OF AIR-GAS INTERFACE

For the Through-Flow configuration, two air-gas interfaces are present. One begins from the EI opening and finally exits to the EO. The second interface begins at the opening of the AI port and propagates through the channels and is either exhausted through the EO port or recycled into the AO port for the next cycle. This exhaust gas that leaks into the next cycle is known as the exhaust gas recirculation (EGR).

For the Reverse-Flow configuration, only one interface exists which starts at the EI opening and exits (under normal scavenging conditions) to the EO port.

The code calculates the position of the gas-air interface at all zones which helps analyze the scavenging ability of the design geometry and the operating condition. Another

important factor to be calculated for either of the flow configurations is the amount of EGR. The calculation of the air-gas interface provides the opportunity to understand the behavior of the air-gas interface with respect to pressure and temperature conditions and subsequently allowing the selection of an operation point with greater tolerance for a shift of the interface without affecting the output pressure and air quality.

The calculation procedure for the Through-Flow configuration is given below.

x_1 to x_6 define the first interface and x_7 to x_{10} define the second interface.

(x_{20}, x_{21} and x_{22} are used to calculate the second interface position if exhaust gas recirculation is present.)

FIRST INTERFACE

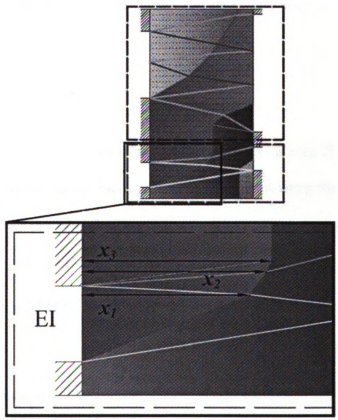

Fig. 19 High pressure region (Inset) first interface distances in HP region

For the position of the first interface (Fig. 19), the flow velocity has been previously calculated for both mediums (air and gas) and is equal in the same zone but the local speed of sound varies with temperature and thus influences the wave propagation speed in different media.

As a convention, the code measures all lengths from the left and assumes waves propagating from left to right have positive velocity and vice-versa, the absolute values of the velocity are considered for the computation as all measured lengths are positive.

It would take the same time for S1 to travel the complete length of the wave rotor and the returning wave S2 to travel in air as it would take the exhaust gas to travel into the channel (see Fig. 11). S1 induces a flow velocity u_{II} while S2 has to travel against u_{II} which ultimately slows down the flow. This can be clearly seen in the equation listed below.

$$\frac{x_1}{u_{II}} = \frac{L}{|w_{S1}|} + \frac{L - x_1}{|w_{S2\_air}|} \tag{39}$$

Equation (39) gives us the position of the gas-air interface in zone *II*. Subsequently, we can calculate the position of the interface in zone *III* by correlating that the time it would take for both, shockwave S2 and expansion wave E1 to propagate in exhaust gas would be the same as the time needed for the interface to travel the distance $x_2 - x_1$ at a fluid flow velocity of u_{III} (*a proof of a similar calculation has been described in the second interface*).

$$\frac{x_2 - x_1}{u_{III}} = \frac{x_1}{|w_{S2\_gas}|} + \frac{x_2}{|w_{E1\_h\_gas}|} \tag{40}$$

Where,

x_1 interface position due to S1

x_2 interface position due to head of E1

L length of the wave rotor channel

u_{III} fluid flow velocity in zone *III*

w_{S1} wave propagation velocity for S1

w_{S2_air} wave propagation velocity for S2 in air

w_{S2_gas} wave propagation velocity for S2 in gas

$w_{E1\_h\_gas}$ wave propagation velocity for E1 head in gas

x_3 is created by the tail wave of E3 and hence the position is calculated as

$$\frac{x_3 - x_2}{\left(\frac{u_{III} + u_{IV}}{2}\right)} = \frac{x_3}{\left|w_{E1\_t\_gas}\right|} + \frac{x_2}{\left|w_{E1\_h\_gas}\right|} \tag{41}$$

Since the tail wave induces a fluid flow velocity u slower than the head wave, the average velocity between Zone *III* and Zone *IV* is taken as the flow velocity in the region between the head and tail waves of E1.

x_4 is created by the wave interaction in Zone *IV*. As Zone *IV* is considered a static zone, the position of the air-gas interface remains unchanged. Hence, $x_4 = x_3$.

x_5 and x_6 complete the path for the first gas-air interface extending into the low pressure region and exhausting into the EO port. x_5 is created due to the Expansion

Wave E2 which is a result of the sudden opening of the EO port. A strong expansion is generated by E2 which draws the air-gas interface towards the EO port.

x_6 is the final position of the first air-gas interface and is on the right side end which is equal to the length of the wave rotor. $(x_6 = L)$

SECOND INTERFACE

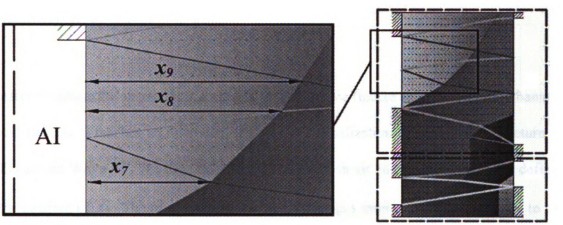

Fig. 20 Low pressure region (Inset) Important distances of second interface in LP region

For the low pressure region, the second interface begins at the AI port opening. x_7 is the first interaction of the second air-gas interface (Fig. 20). As E3 propagates only in exhaust gas, it covers the length of the channel and returns as pressure wave P1. P1 travels in exhaust gas all the way till x_7. Equating the times of propagation, x_7 can be calculated as

$$\frac{x_7}{u_{VI}} = \frac{L}{|w_{E3}|} + \frac{L - x_7}{|w_{P1\_gas}|} \tag{42}$$

Where,

x_7 interface position due to P1

u_{VI} fluid flow velocity in Zone *VI*

w_{E3} wave speed of expansion wave E3

w_{P1_gas} wave speed of pressure wave P1 in exhaust gas

A similar convention is used for all the subsequent waves and interface positions and hence will not be explained in detail.

After P1 enters the air medium, it travels to the left side (intake side) of the rotor channels and because it reaches an open end, the pressure equalization process makes it return as Expansion Wave E4. The time taken for P1 to travel in air and E4 to travel in air defines the position of x_8. The time taken for the second air-gas interface to shift from x_7 to x_8 is equal to the time for the waves P1 and E4 to travel in air.

$$\underbrace{\frac{x_7}{u_{VI}} + \left\{\frac{x_8 - x_7}{u_{VII}}\right\}}_{\text{time for shift of air–gas interface}} = \frac{L}{|w_{E3}|} + \frac{L - x_7}{|w_{P1\_gas}|} + \underbrace{\left\{\frac{x_7}{|w_{P1\_air}|} + \frac{x_8}{|w_{E4\_air}|}\right\}}_{\text{additional time for wave propagation}} \qquad (43)$$

Subtracting equation (42) from (43), we get

$$\frac{x_8 - x_7}{u_{VII}} = \frac{x_7}{|w_{P1\_air}|} + \frac{x_8}{|w_{E4\_air}|} \qquad (44)$$

x_8 can be calculated using this equation.

Expansion wave E4 continues to propagate after x_8 in exhaust gas with a higher wave speed due to the elevated temperature and also being assisted by the induced flow velocity u_{VII}. When E4 reaches the open end at the EO port, it reverses its direction to propagate as pressure wave P2. As P2 is traveling opposite to the induced flow velocity, it tends to slow down the fluid flow velocity for the next zone i.e. zone *IX*. Using a procedure similar to the calculation above, we can calculate x_9 by equation (45).

$$\frac{x_9 - x_8}{u_{VIII}} = \frac{L - x_8}{\left|w_{E4\_gas}\right|} + \frac{L - x_9}{\left|w_{P2\_gas}\right|} \tag{45}$$

After x_9, P2 propagates in air and hence at a slower speed which is reduced even more due to its propagation against the fluid flow velocity u_{VIII}. As P2 traverses the length of the rotor channel, its arrival at the intake side governs the AI port closing time. Due to the pressure equalization process, P2 reverses its direction and propagates as expansion wave E5 and travels towards the EO port. Using the time for the shift of the interface with the time for the wave propagation, we can calculate x_{10} by equation (46).

$$\frac{x_{10} - x_9}{u_{IX}} = \frac{x_9}{\left|w_{P2\_air}\right|} + \frac{x_{10}}{\left|w_{E5\_air}\right|} \tag{46}$$

The calculations for x are terminated if any value of x is equal the length of the wave rotor channel or exceeds it. After this point, subsequent values of x are omitted and the waves are assumed to propagate in a single medium between the AI and EO port.

If $x_{10} < L$, exhaust gas would be recirculated to the next cycle and needs to be accounted for. The code calculates the position of x_{10} and recalculates the position of the interface, this time, with zone *I* containing both air and gas components. In an operating condition where EGR is present, the second interface extends into zone *I* from zone *X*. Here, as it is in a static zone (zero velocity), the interface position remains constant till it interacts with S1. Its progressive interactions with S1 and S2 are calculated and by this method, the second interface is displayed.

As an example, for the Operating Point 1 (without EGR),

P1	0.98 bar
P2	2.40 bar
P3	1.80 bar
P4	1.02 bar
T1	300 Kelvin
T3	1100 Kelvin

Table 3 Operation Point 1

the values of x are tabulated below

x	Value (mm)	x	Value (mm)
x_1	60.2	x_6	93
x_2	73.7	x_7	37.9
x_3	74.1	x_8	69.6
x_4	74.1	x_9	74.4
x_5	81.9	x_{10}	93

Table 4 Values of x for Operation Point 1 (Yellow : interface 1 ; Green : Interface 2)

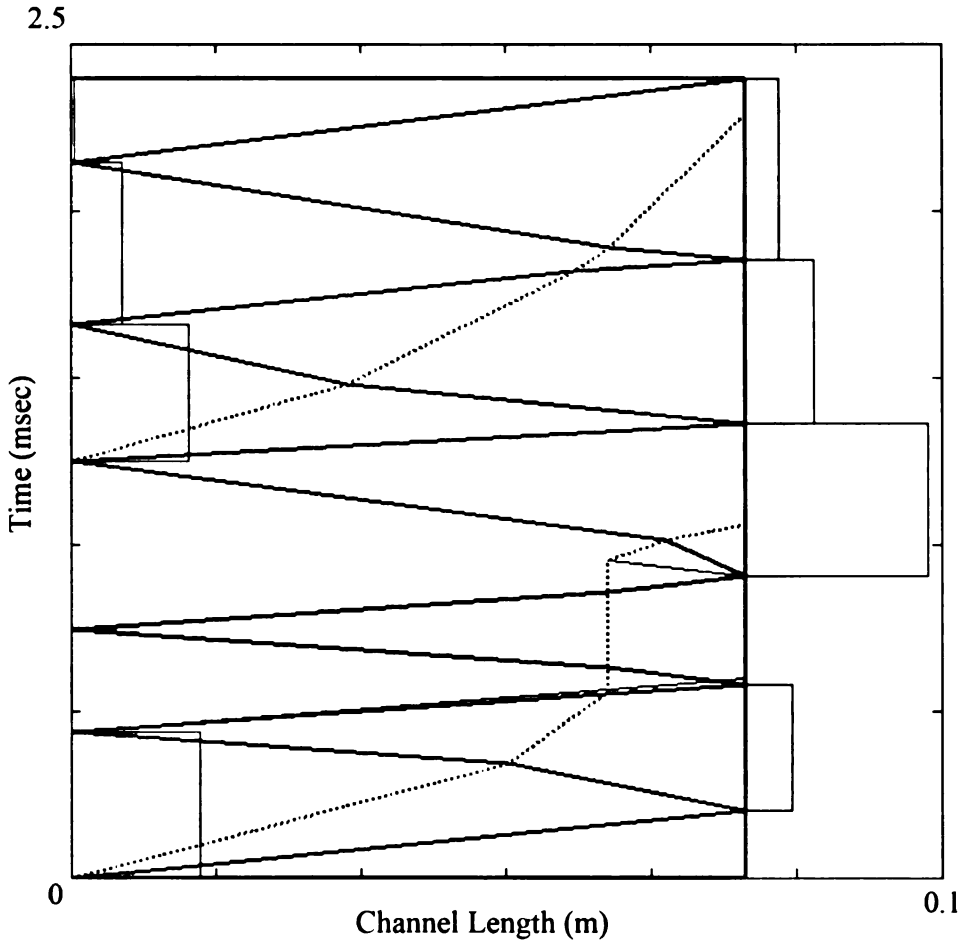

Fig. 21 Output of 1D Algebraic code for Operation Point 1

3.6 OUTPUT NOMENCLATURE

The output for the code is presented graphically as the wave diagram in Fig. 21. On the x-axis, we have the length of the rotor (which is 93 mm as the geometry is computed for the CX-93). The y-axis is the total time for the wave interactions which begin at the EI port opening and end at the closing of the EO port. As the distance traveled by each wave is the length of the channel, the time is computed for each wave and plotted graphically to

show the total time needed for the completion of the complete process (normally between 2-3 milliseconds).

The blue lines represent the wave interactions. The red lines represent the air-gas interfaces. The black lines are the set of virtual waves assumed to compute the opening of the EO port. The green lines show the scaled zone averaged velocities.

The cyan colored line at the top (in zone *X*) shows the velocity head converted from the residual pressure after E5. The objective is to have a fluid flow velocity close to or equal to zero for zone *X* as it has to match the initial state of cycle (zone *I*).

CHAPTER 4

CODE VALIDATION

The operating conditions were studied in two stages. The first stage, the preliminary data set (Table 5) had a range of values which could be easily demonstrated in the Turbomachinery Laboratory without the use of special safety devices. The second stage, the exhaustive data set, was a set of boundary conditions that accounted for a very large range of pressures (not shown here) which provided data which could easily be interpolated to optimize for a specific device.

The boundary conditions of the preliminary data set are given below.

Property	Unit	Symbol	Max	Min	Discretization step
Air Inlet pressure	Bar	P1	0.92	1.02	10 kPa
Air Outlet pressure	Bar	P2	1.5	2.2	10 kPa
Exhaust Inlet pressure	Bar	P3	1.35	1.8	10 kPa
Exhaust Outlet/Backpressure/ Turbine Inlet Pressure	Bar	P4	0.92	1.25	5 kPa
Air Inlet Temperature	Kelvin	T1	300		0
Exhaust Inlet Temperature	Kelvin	T3	1100		0

Table 5 Preliminary Data Set

In previous research on wave rotors [18], [20] in both Through Flow and Reverse Flow configurations, it was observed that the EGR was very sensitive to the backpressure (P4). This is the prime reason why P4 was studied to the greatest extent to document its effect on the performance of the wave rotor.

After the results from the preliminary data set were studied, an operating condition was chosen to be computed by the code. The resulting output of porting geometry and rotor speed would be applied as inputs to two different kinds of codes to validate the results. A commercial one dimensional code for powertrain applications, GT-POWER was used for the preliminary validation owing to its speed of computation as compared to a CFD code. Further, this geometry would be validated in a two dimensional CFD model setup in FLUENT which would provide results with very high accuracy at the cost of computation time. The objective was to assess the accuracy of the 1D algebraic code and study the benefits and shortcomings of its use.

4.1 GT-POWER MODEL

GT-POWER (by Gamma Technologies Inc.) is an unsteady, compressible flow simulation package which is used to simulate the gas flow in induction and exhaust systems for internal combustion engines. It is a tool widely used in the automotive industry for powertrain development. The software functionality and versatility is what allows the user to customize it for a variety of applications.

GT-POWER has been used previously in modeling a reverse flow wave rotor configuration for a 1.5 litre Renault test engine [18]. The success of its use provided ample opportunity for validating the 1D algebraic code.

Fig. 22 shows the basic layout of a single channel of the wave rotor in a reverse flow configuration. The method applied to model the wave rotor is by considering each channel to be a duct and by using a timed valve at the ends to generate the appropriate timing for the opening and closing of each channel with respect to the porting geometry.

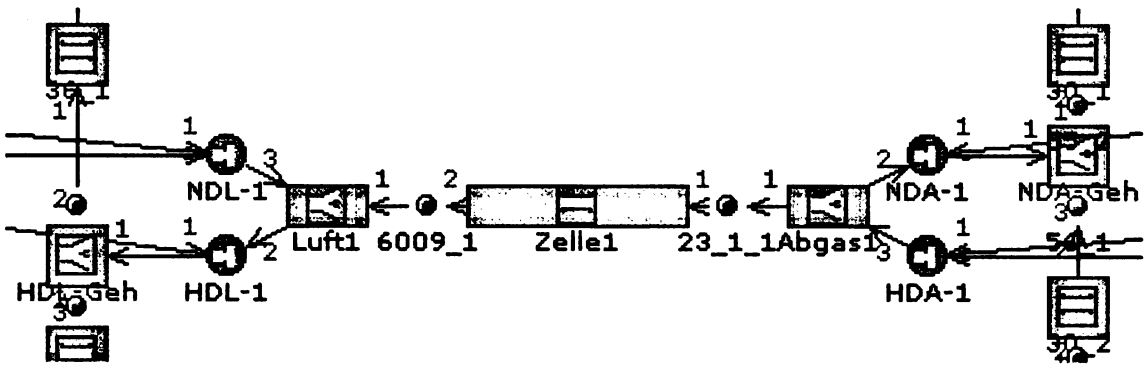

Fig. 22 GT-POWER model layout of ducts for reverse flow configuration

A combustion chamber can be modeled in GT-POWER as a diesel or gasoline engine which is sized to produced the required mass flow rate. This behaves as the Exhaust Inlet with a throttled pipe to match the Air Outlet exit mass flow.

A sequential set of controllers are added to the valves which open or close the channel to the correct pressure boundary. The valves have a slew rate of 1° of crank angle rotation from closed to fully open to simulate the sudden opening of the channels to a port. The controllers actuate the opening of every subsequent port with a fixed time delay to ensure a smooth opening of the channel to each port.

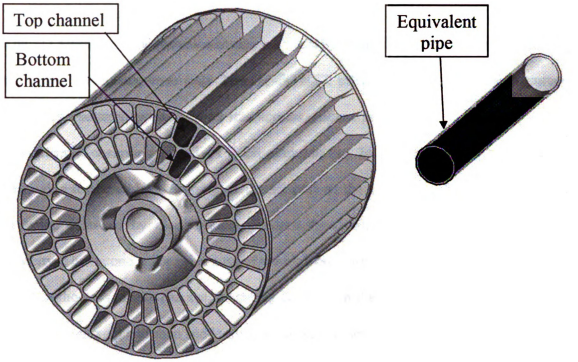

Fig. 23 Conversion of channels of wave rotor to equivalent duct in GT-POWER

As the COMPREX® has two sets of 34 concentric channels, the total flow area was calculated and then converted to an equivalent pipe diameter (Fig. 23) by the following calculation.

$$A_{equivalent\ pipe} = A_{top\ channel} + A_{bottom\ channel}$$

$$\frac{\pi D^2}{4}\ \text{mm}^2 = (65.73 + 50.63)\ \text{mm}^2$$

$$D = 12.17\ \text{mm}$$

(*Note : The area of the channels were calculated from the CAD model*)

4.2 GT-POWER RESULTS

The 1D algebraic code provides results on a zone averaged velocity which is visible in the output plot of the code (Fig. 21). GT-POWER provides results of greater accuracy and gives a better view of the wave interactions within a port.

For example, observing the GT-POWER output in Fig. 24 for the EI port, we can see the spike due to the sudden opening of the EI port to the channels which are at a lower pressure, followed by a subsequent pressure equalization process which reduces the velocity. The second spike is because of the high pressure in the EI port which propagates the first shockwave. We can see the steady decrease in the velocity as the pressure in the channels builds up and then suddenly goes into the negative region due to the expansion wave E1. As the 1D algebraic code does not account for leakages, there is a possibility of a slight mistiming of the wave due to the change in the pressure ratio. This can be seen by the negative spike and it would be preferable to close the port earlier to avoid any backflow into the EI port.

Fig. 24 and Fig. 25 show the comparison between the outputs from the 1D Algebraic Code and the GT-POWER simulation. The results are taken at a given instant that the simulation results have converged in GT-POWER, which would mean a steady wave pattern is present between the channels.

The GT-POWER results clearly show the spikes in velocity when the area of a channel begins to reduce which is very similar to the velocity or mach number observations at an exhaust valve for an IC engine. Nonetheless, the average value of the flow velocities for all the ports are in close agreement with the 1D algebraic code.

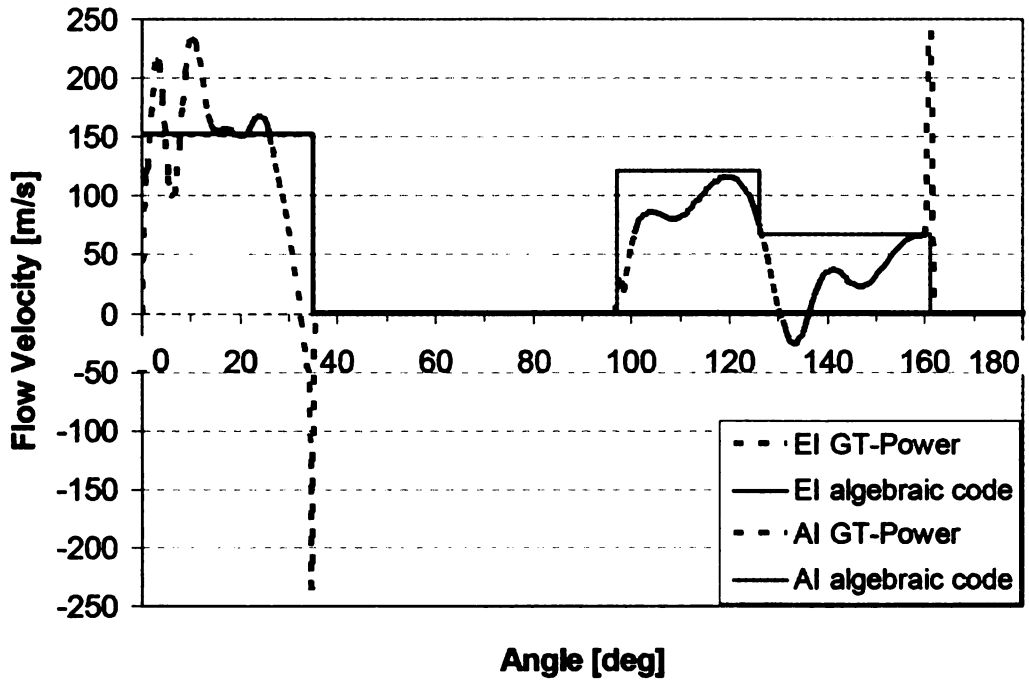

Fig. 24 Comparison of flow velocities at EI and AI port

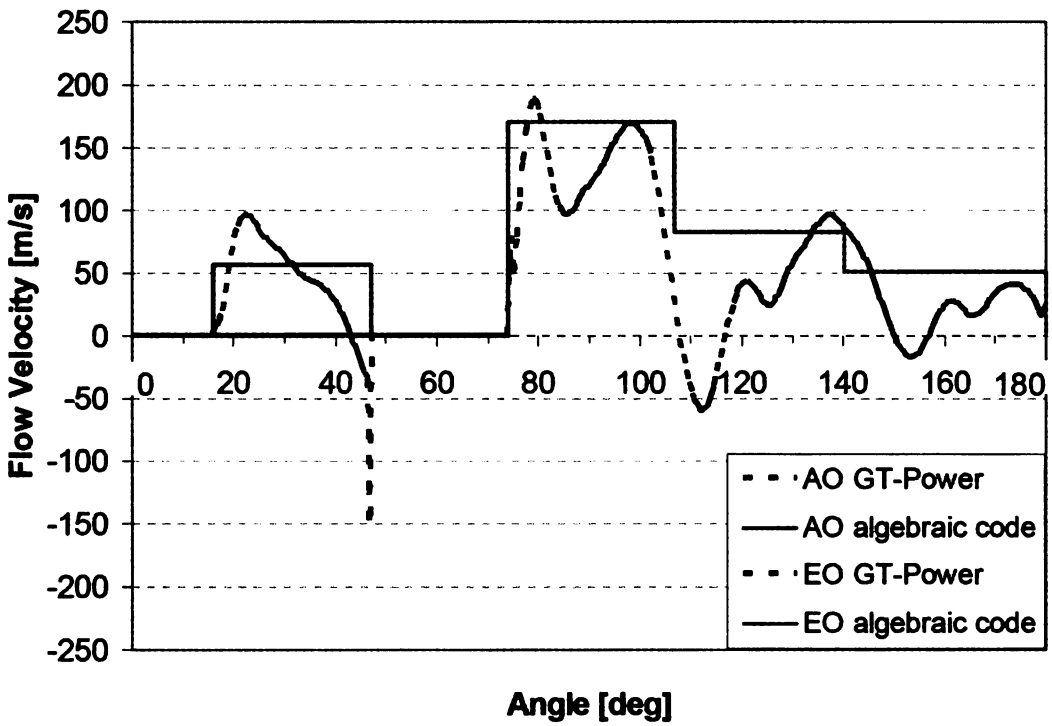

Fig. 25 Comparison of flow velocities at EO and AO port

4.3 FLUENT® MODEL

FLUENT® 6.2 is a commercial computational fluid dynamics package which can run simulations in two and three dimensional space for unsteady, single and multi phase flows.

FLUENT® is run in conjunction with GAMBIT which is the meshing tool supplied with FLUENT®. A design geometry is first modeled in GAMBIT, meshed appropriately and then imported into FLUENT® for the solution process. FLUENT® allows us to study the effect of secondary waves which is something the 1D algebraic code cannot do. Due to the secondary waves generated by the pressure and expansion waves, the entire wave process in the low pressure region is very complex. The objective of modeling the wave rotor in a 2D model was to be able to study the accuracy of the 1D Algebraic code after accounting for the code's assumptions.

The 2D model was also set up to account for leakage spaces [25] between the end plates and the rotor channels. This was done to provide a good estimate of the effect of the leakage space on the wave pattern.

A range of leakage space values were tested to achieve a steady pressure wave pattern. When tested for a leakage space of 0.5mm, the pattern deteriorated considerably and for the same reason, those results were excluded. Finally a spacing of 0.25mm was agreed upon because a clear wave pattern was visible while the spacing was an achievable value in the manufacturing of the test rig. Values lower than 0.25mm would be extremely difficult to maintain at the test rig when the rotor is operating at temperatures of near 1000K and spinning near 15,000 rpm.

For this body of research, the coupled, laminar, 2D double precision (2ddp) solver was used (3D CFD models are extremely expensive for computation and were not included). The model was scaled to millimeter scale and for the solution and the PISO (Pressure Implicit Splitting of Operators) technique was used. All the unsteady time dependent flows were analyzed at a time step of 1 microsecond (1×10^{-6} seconds).

As CFD computations are quite expensive, to save time, only a half model of the wave rotor was considered (i.e. 17 channels). This is an acceptable technique as the analysis is for a two cycle through flow configuration and a periodic boundary condition had been applied to the model.

4.3.1 MESHING STRATEGY

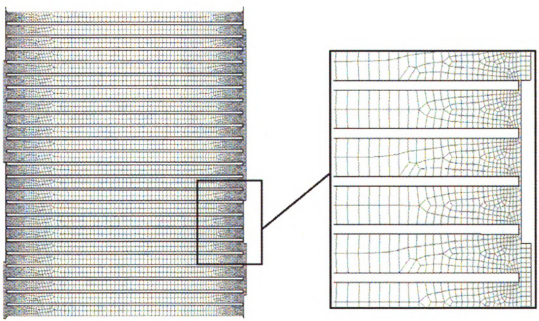

Fig. 26 GAMBIT Mesh for through flow wave rotor configuration. (Inset) Enlarged view of the fine mesh used at ports and leakage spaces

The GAMBIT geometry model (Fig. 26) of the wave rotor was created in millimeter scale and was meshed using a quad element scheme using a bi-exponent elemental distribution. The reason for using such a scheme was that the analysis of the leakage space between the rotor and the end plates and the flow in each port was critical for validating the code. The bi-exponent distribution increased the mesh density at the channel ends and made the inner regions sparse which allowed the detailed study of flows in the port while saving computation time. The mesh used for the computation is shown in Fig. 26.

From the computed RPM from the code, the mesh velocity was computed for the average flow radius r_{avg} as follows,

$$v = r_{avg}\,\omega \qquad (m/s) \tag{47}$$

But $\omega = \dfrac{2\pi N}{60} \quad (r/s)$

$$r_{avg} = \left(\frac{R_{outer} - R_{inner}}{2}\right) + R_{inner} \quad (mm)$$

$$\therefore v = \left(\left(\frac{R_{outer} - R_{inner}}{2}\right) + R_{inner}\right) \times \frac{2\pi N}{60} \quad (m/s)$$

Substituting the appropriate values,

$$v = \left(\left(\frac{46.5\times10^{-3} - 22.3\times10^{-3}}{2}\right) + 22.3\times10^{-3}\right) \times \frac{2\pi\times12600}{60} \quad (m/s)$$

$$= 45.4 \quad mm/s$$

$$\approx 0.045 \quad m/s$$

Using this mesh velocity, the results were computed till a distinct wave pattern was visible in the pressure contour plots.

A very important part of the meshing was the choice of wall length. It was required for the wall after the Exhaust Outlet closing to be extended by a length greater than the width of a single channel due to the short circuiting of the Exhaust Inlet port with the Exhaust Outlet port due to the periodicity condition. If this precaution is not taken, a pressure wave pattern gets recorded in which the EO port is influenced by the EI port directly and hence interferes with the last Expansion Wave (E5).

4.4 FLUENT RESULTS

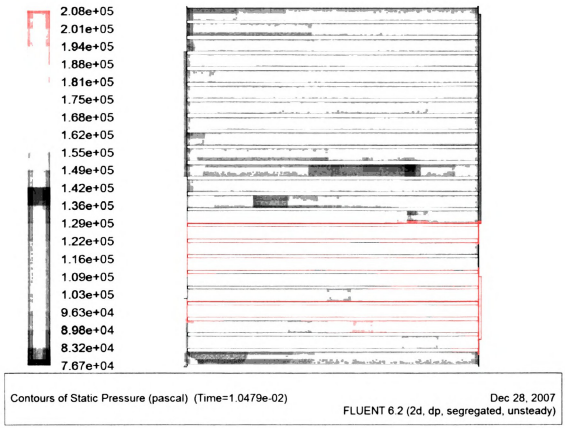

Fig. 27 Pressure contours from FLUENT simulation

In Fig. 27 we see the pressure contours generated by a steady wave pattern in the channels where the zones are clearly visible. Just after the first channel, because of the sudden opening of the EI port, there is an increase in the pressure. The first shockwave is timed to reach the outlet side just before the opening of the AO port which is visible with the increasing gradient towards the port. The second shockwave generates the increased pressure in the channels (zone *III*) which is seen in the gradient increase till AO closing. The high pressure region is distinctly visible all the way till the end of zone *IV*. Due to the strong expansion wave E2, we can see the pressure reduction of the channels to the low pressure region. E2 is timed to reach the AI opening after which a series of pressure and expansion waves traverse the channels before the closing of the EO port.

The waves (as illustrated in the results section, Fig. 48) and the difference between the high and low pressure region can be clearly noticed in the pressure contours and validates the assumptions of the 1D algebraic code.

It is also important to study the temperature (Fig. 28) of the fluid because the local speed of sound is influenced by the fluid temperature. Also, as there is no physical boundary between the two fluids, the only way to distinguish between air and exhaust gas is the temperature difference. As the wave exchange process is completed in a very short period (between 2 to 3 milliseconds), the time for diffusion and heat transfer between the two media is low. The temperature contour plot gives a fairly accurate picture of the behavior of the air-gas interface.

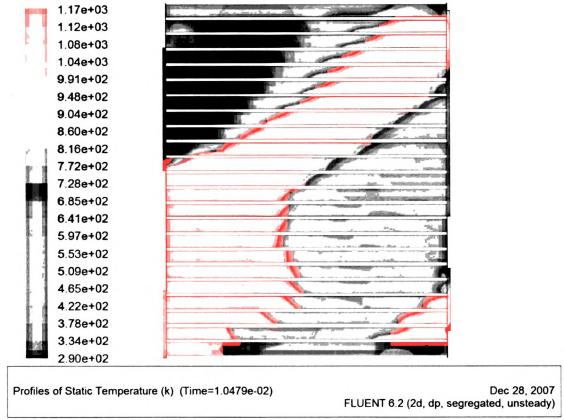

Fig. 28 Static temperature contours from FLUENT simulation

Fig. 29 shows the velocity vector plot for the fluid flow velocities. The velocity vector plot is used to study how well the waves are timed with respect to the ports. Any mistiming would lead to anomalous behavior at the ports and change the mass flow rates. As seen at the ports, the velocities vary with respect to each pressure/expansion wave. Looking at the EO port, we can see a steady reduction in the flow velocities. As a strong expansion wave (E2) propagates at EO opening, the fluid flow velocity would be high which is clearly visible. As the subsequent wave interactions are weak due to the low pressure ratio, the influence on the port velocities reduce and the velocities steadily decrease.

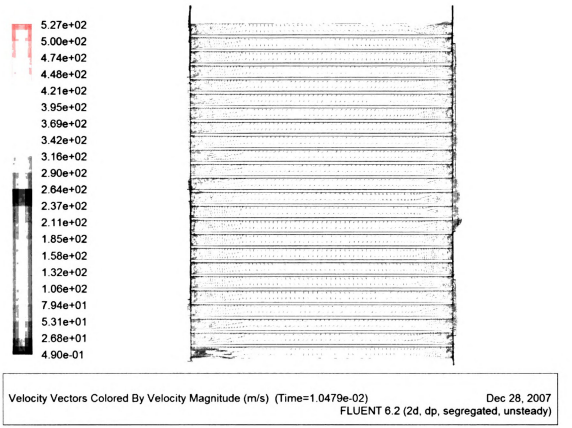

Fig. 29 Velocity vector plot from FLUENT simulation

It is a target of the 1D Algebraic code to exhibit similar trends in the fluid flow velocities. The accuracy of the FLUENT result is extremely high as the velocity is computed at each grid cell of the mesh as compared to the zone averaged velocity of the code.

DEVIATION OF FLOW (BACKFLOW)

Due to the assumption of the 1D algebraic code, it was expected that results higher than practically possible would be achieved. As the leakage reduces the pressure, there is also a possibility of mistiming the waves which would lead to slightly anomalous behavior of the pressure wave machine. This phenomenon is evident in the Air Outlet port (Fig. 30).

Due to shockwaves S1 and S2, the flow in the AO port is in the outward direction but due to the mistiming of the wave, the expansion wave (E1) is supposed to define the closing of the AO port. As E1 reaches the AO port earlier than the closing time, it creates a backflow (red dotted demarcation) which creates a detuned point for the wave pattern. The backflow reduces the mass of the pressurized air going to the combustor inlet or collector and also creates a pressure wave that propagates towards the inlet side before the closing of the AO port. This causes the air-gas interface to shift backwards (towards the inlet side) which is an undesirable condition. This could lead to an increase in the localized heating of the rotor due to exhaust gas retention which can cause undue thermal stresses. This detuned pressure wave would also increase the exit time for the exhaust gas which could lead to an increase in the EGR for the cycle. This example illustrates why it is critical to choose the correct porting geometry for the pressure wave process.

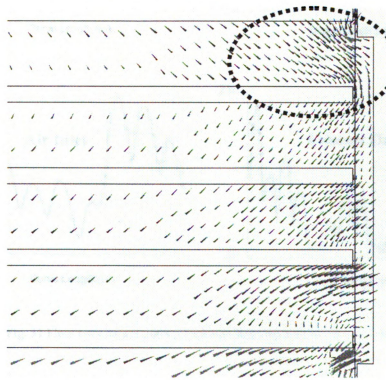

Fig. 30 Velocity vector plot of flow in Air Outlet (AO) port

VELOCITY OUTPUT AT EACH PORT

Fig. 31 shows the fluid flow velocity profile at each port. There is a noticeable influence of the channel walls on the output flow at the port. The crests in each velocity profile correspond to the number of channels open to the port (Fig. 29).

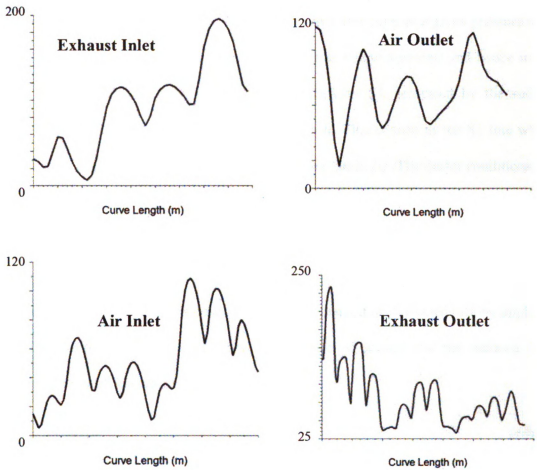

Fig. 31 Flow velocities at ports (Clockwise from top left) EI, AO, EO, AO

4.5 CHARACTERISTIC DIAGRAM

Using the method of characteristics [24], the through flow configuration is represented in the state diagram (Fig. 32). The state diagram is a plot of normalized pressure $\left(p/p_0\right)^{\frac{\gamma-1}{2\gamma}}$ versus normalized velocity $\left(u/a_0\right)$ and the origin for the is $(0, p_{atm})$.

An assumption applied in the state diagram is that shockwaves can be approximated as pressure waves as they propagate with nearly the same velocities at a given pressure ratio [17]. State *I* is the pressure of the channels (which is below ambient) and hence in the fourth quadrant of the diagram. Due to the shockwave S1 generated by the sudden opening of the EI port, the state changes from *I* to *II*. This is seen as the S1 line which links the initial condition (state *I*) to the EI pressure (state *II*). The outlet conditions are considered as constant pressure boundaries while the inlet pressure boundaries are defined at their stagnation pressures but decrease as the induced velocity increases. This maintains the energy balance of the system.

Change of state by the waves is described using the method of characteristics by applying the relationship between state quantity (local speed of sound) and the induced flow velocity in the well known form,

$$da = \pm\frac{\gamma-1}{2}du \tag{48}$$

For the change of state by expansion/pressure wave, the waves propagating between state 1 (initial) and 2 (final) and traveling towards the right can be shown by using the normalized state quantities,

$$\frac{a_1}{a_0} - \frac{\gamma-1}{2}\cdot\frac{u_1}{a_0} = \frac{a_2}{a_0} - \frac{\gamma-1}{2}\cdot\frac{u_2}{a_0} \tag{49}$$

Where,

a_0 = Reference speed of sound at reference pressure p_0

For a wave propagating between State 1 and 2 and traveling towards the left follows,

$$\frac{a_1}{a_0} + \frac{\gamma-1}{2}\cdot\frac{u_1}{a_0} = \frac{a_2}{a_0} + \frac{\gamma-1}{2}\cdot\frac{u_2}{a_0} \tag{50}$$

As pressure waves work on the same theory as expansion waves, we can use equation (48) – (50) to describe both.

Equations (48) - (50) are written for waves propagating in a single medium. In the wave rotor the pressure or expansion waves propagate in mediums of different temperature and composition (hot exhaust gas and cold fresh air) and according to the state characteristics, a wave propagating in exhaust gas yields equation (51),

$$d\left(\left(\frac{p}{p_0}\right)^{\frac{\gamma_{air}-1}{2\gamma_{air}}}\right) = \pm\frac{\gamma_{air}-1}{2}\cdot\frac{a_{0air}}{a_{0gas}}\cdot\frac{\gamma_{gas}}{\gamma_{air}}d\left(\frac{u}{a_{0air}}\right) \tag{51}$$

Where,

a_{0air} = Reference speed of sound in air at ref. pressure p_0

a_{0gas} = Reference speed of sound in gas at ref. pressure p_0

From equation (51), it can be seen that the magnitude of the induced flow velocity differs for gas and air. In the introduced algebraic code, if the waves propagate both in gas and

in air the average of the induced flow velocities has been used for estimation of the flow velocity in particular state.

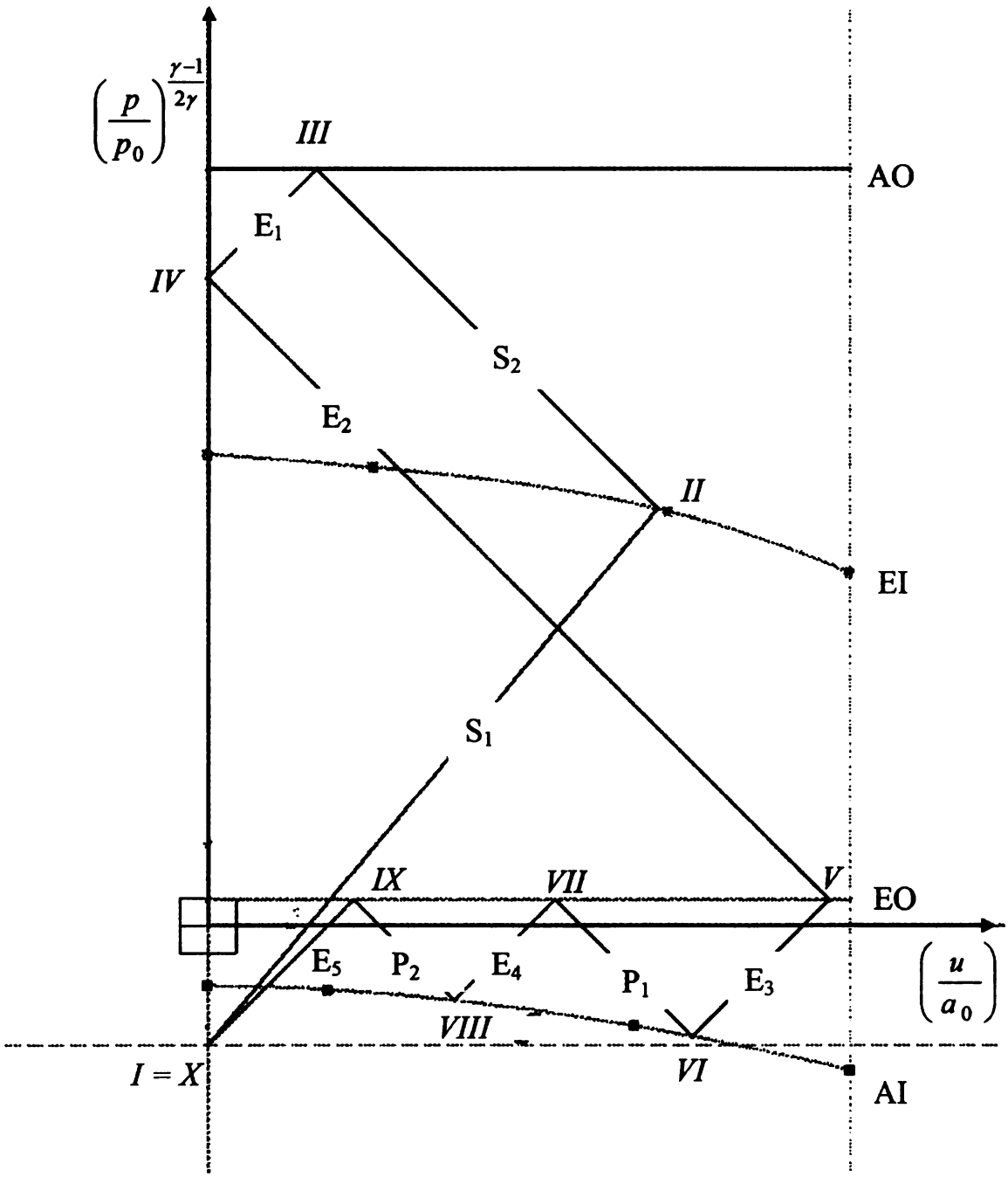

Fig. 32 Characteristic diagram for a through flow configuration with all waves and states [20]

4.6 CHARACTERISTIC DIAGRAM PARAMETRIC MODEL

To understand the trends in such a system, a parametric model of the characteristic diagram was created. This would provide the opportunity to study the pressure wave process qualitatively. The parametric model allows the user to fix all but two of the reference pressures and then vary a single reference pressure to observe the effect on the pressure/expansion waves and the other unconstrained pressure. It is also within the scope of the model to fix the velocities of each wave as long as the propagation is respected. The change in direction of each subsequent wave is done while respecting the medium it propagates in. Waves travel faster in a medium of higher temperature and hence the angle for a wave propagating in exhaust gas is more acute than a wave propagating in air.

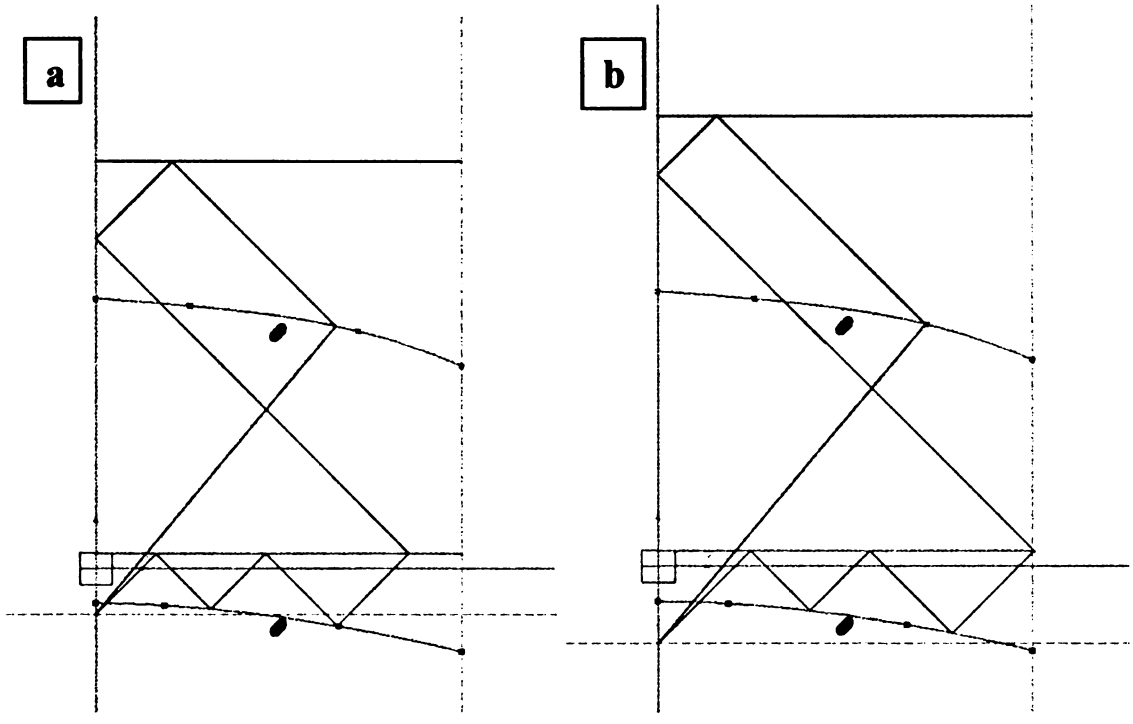

Fig. 33 Effect of variation of reference pressure on AO pressure with other pressure boundaries held constant

One drawback of the parametric model is that it cannot estimate the exhaust gas recirculation at that operating condition but still serves as a very efficient tool to study the pressure wave process qualitatively.

For example, in Fig. 33 we see the variation of AO pressure if the reference pressure of the channels (dotted line) is changed. For this simulation, AI, EO and EI pressures were fixed values while the pressure in the channels was reduced from being very close to AI pressure (Fig. 33 (a)) to being much lower than AI (Fig. 33 (b)). This large decrease in pressure inside the channels leads to much higher zone velocities and an elevated AO pressure. This is because such a pressure condition would result in a very strong shockwave S1. In a similar way, any pressure or wave can be constrained and its influence on other waves can be studied.

CHAPTER 5

RESULT ANALYSIS

The 1D algebraic code was run for a wide range of pressures to find all the possible variations and to analyze the trends influenced by the boundary conditions. The results were filtered to allow a 10% mass balance between the Exhaust Inlet (EI) port and the Air Outlet (AO) port and also between the Air Inlet (AI) port and Exhaust Outlet (EO) port.

5.1 PERFORMANCE MAPS

The parameters studied to maximize performance of the wave rotor were the pressure ratios $\frac{P_4}{P_1}$, $\frac{P_2}{P_1}$, $\frac{P_2}{P_3}$, Exhaust Gas Recirculation and mass balance.

- P_4/P_1

  $\frac{P_4}{P_1}$ is known as the **Turbine Inlet Pressure Gain**. This is also the pressure ratio of the low pressure region and governs the strength of the wave interactions and the backflow into the channels. The increase in $\frac{P_4}{P_1}$ would provide a greater pressure at the inlet of the turbine which would reflect in the turbine speed as there would be a greater pressure to expand over. The limitation on this factor is that an increase in

$\frac{P_4}{P_1}$ leads to an elevated back pressure and consequently, increased recirculation. The EGR dilutes the air quality at the AO port and also increases the total temperature of the wave rotor.

- P_2/P_1

$\frac{P_2}{P_1}$ is known as the **Compression Gain**. The compression gain is a direct representation of the thermodynamic efficiency of the cycle and hence needs to be maximized. To achieve a high $\frac{P_2}{P_1}$ comes at the cost of reducing the AI pressure which reduces the mass flow at AO or increasing the EI pressure which becomes more demanding on the combustor unit.

- P_2/P_3

$\frac{P_2}{P_3}$ is known as the **High Pressure Gain**. It is the parameter that shows the effectiveness of the shockwaves in the high pressure region. $\frac{P_2}{P_3}$ is proportional to the energy transfer between the two fluid media.

- Exhaust Gas Recirculation (EGR)

EGR is the quantity of exhaust gas that does not exit the rotor and is recirculated in

the next cycle. It tends to dilute the quality of air at the AO port and increases the temperature of the outgoing air hence decreasing the density while adding an inert component to the air. This can deteriorate the performance of the combustor and the overall elevated temperatures of the rotor and components could lead to either seizure or failure in the worst case.

- Mass Balance

  As the gas turbine test rig has to be run in a closed circuit mode, it is a design constraint that the combustor air input should be connected to the AO port of the wave rotor while the exhaust of the combustor goes to the EI port of the wave rotor. This makes the mass balance for the High Pressure (HP) region far more critical than that of the Low Pressure (LP) region. For the LP region, as AI can be taken from either a compressor or directly from ambient air, the mass balance is not critical and a surplus of air is normally desirable. A part of the mass entering at AI is compressed and delivered to the AO port while the remaining air mixes with the hot exhaust gas and brings down the average temperature at the EO port. This aids the design process and reduces the cost as high temperature materials do not need to be employed at the EO port.

The results presented in this chapter were computed for an EI temperature of 1100 K. The operation points at which the inlet mass flows (EI, AI) match the outlet mass flows (AO, EO) were found for various pressure gains in high and low pressure parts. Only points at which the state X is similar to state I were taken into consideration (Fig. 11).

The diagram in Fig. 34 presents the influence of the LP pressure ratio versus the HP pressure ratios. As seen here, $\frac{P_4}{P_1}$ is proportional to the high pressure ratios $\frac{P_2}{P_1}$ and $\frac{P_3}{P_1}$ by a non linear relation. A small change in $\frac{P_4}{P_1}$ (increase of 0.01) requires a significant increase in $\frac{P_2}{P_1}$ and $\frac{P_3}{P_1}$ to have enough energy for scavenging of the wave rotor and maintaining the mass balance.

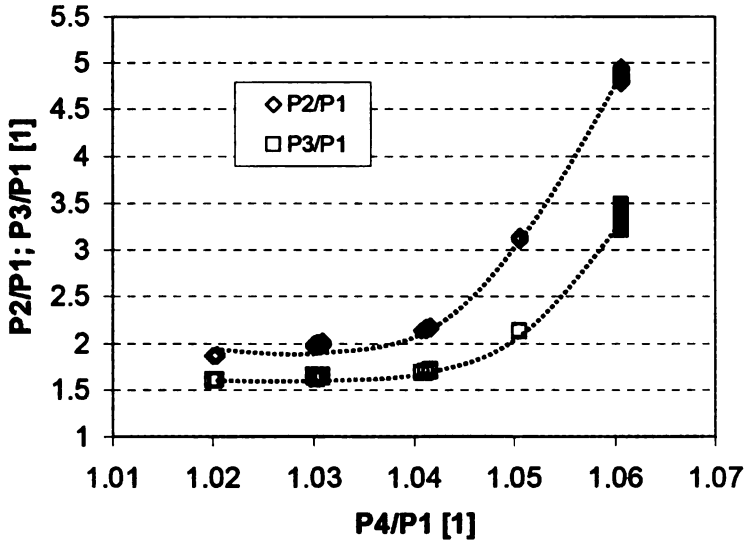

Fig. 34 Influence of pressure gain in LP region on pressure gain in high pressure part

Fig. 35 and Fig. 36 show the behavior of computed internal exhaust gas recirculation over low (Fig. 35) and high (Fig. 36) pressure gains. Only for operation points close to P4/P1 = 1.05 and P2/P1 = 3, there was no recirculation of exhaust gas into the AO port. For P4/P1 < 1.05 there was recirculation by exhaust gas from the previous cycle and for P4/P1 > 1.05 the exhaust gas from EI penetrates directly to the AO port.

From these figures, we can also see how sensitive EGR is to P4. This is expected for the through flow configuration as the chances of exhaust gas retention are higher. It is also expected that the reverse flow configuration will have a wider band of zero EGR conditions because of its natural scavenging ability.

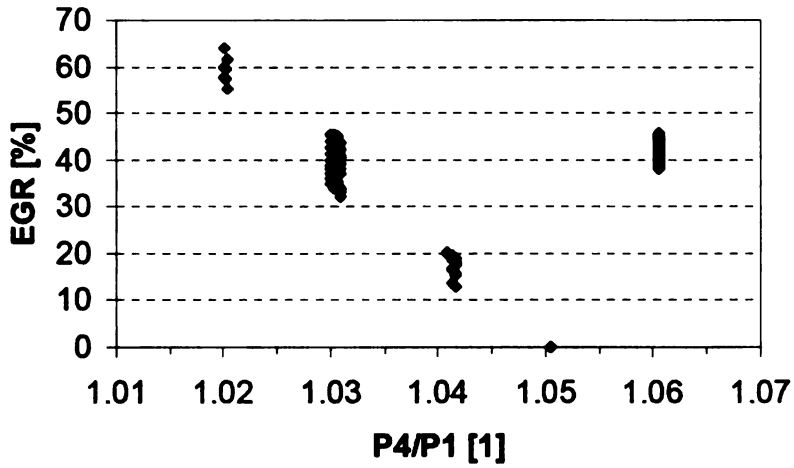

Fig. 35 EGR change with low pressure gain

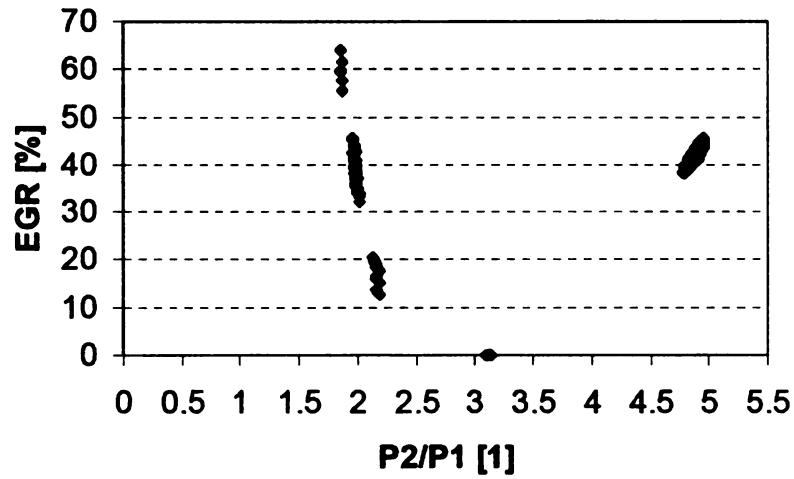

Fig. 36 EGR change with the high pressure gain

Design speed traces are presented in Fig. 37 and Fig. 38. As the time of the cycle reduces with pressure gain decrease, the design speed increases. The rotor speed decreases almost linearly with an increase in P4/P1 while the relation for the high pressure gain to rotor speed closely resembles a hyperbolic function.

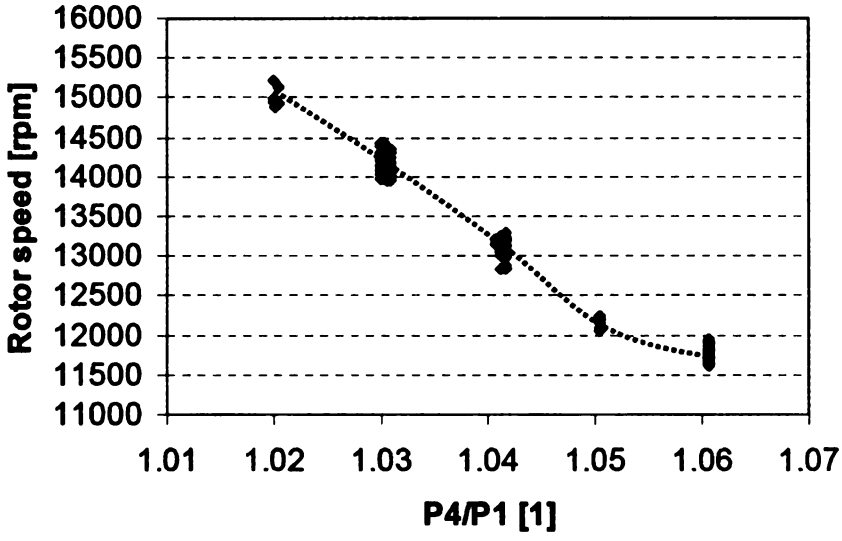

Fig. 37 Design speed variation with the low pressure gain

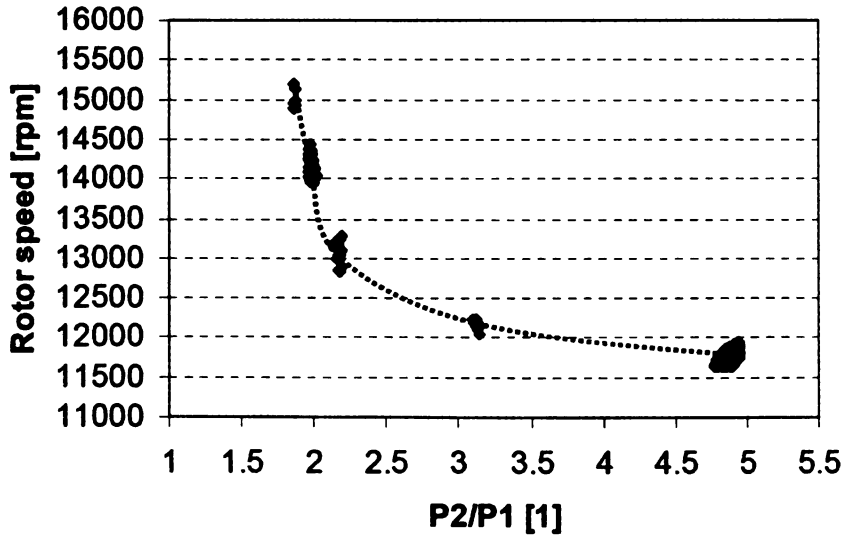

Fig. 38 Design speed variation with the high pressure gain

5.2 PORTING DESIGN

The 1D algebraic code can account for multiple cycles in each revolution. In this study, a two cycle wave rotor is considered and hence the computation of the ports are for 180° of the rotor. The design speed is calculated using the total time for the all the wave interactions.

The results from the analytical code are shown below in graphical form. The area of interest to understand the porting geometry were –

- Width of the ports, and
- Position of ports

and their variation with respect to rotor speed and pressure gains.

5.2.1 **Width of Ports**

This section deals with the variation of the port widths with respect to the rotor speed and compression gain.

(*Note : Most of the plots are created in 3D but are presented in the 2D form for simplified representation. It is easier to study trends with 3D plots as more parameters can be accommodated. A few examples can be found in Appendix B.4.*)

Fig. 39 shows the trend of included angle of the ports with respect to speed. It is clearly visible that for a variation in rotor speed of 4000 rpm, both EI and AO port vary by about 8°. This can create a problem for control because of the minute variations for porting to maintain the tuned pressure wave process.

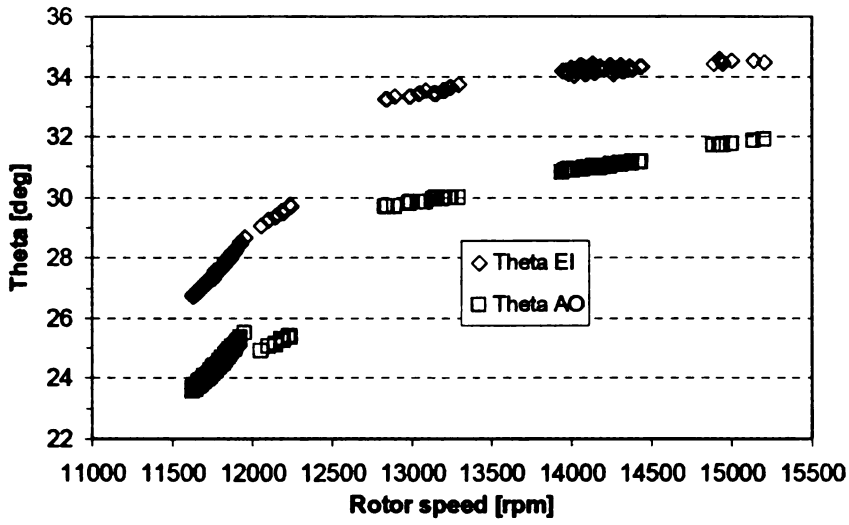

Fig. 39 Change of width of high pressure ports with design speed

Fig. 40 shows the variation of the EI and AO port angles with respect to the compression gain. The decrease in port width is visible with an increase in the pressure ratio. Correlating the results from Fig. 39, if the compression gain has to be increased, the rotor speed will need to be reduced.

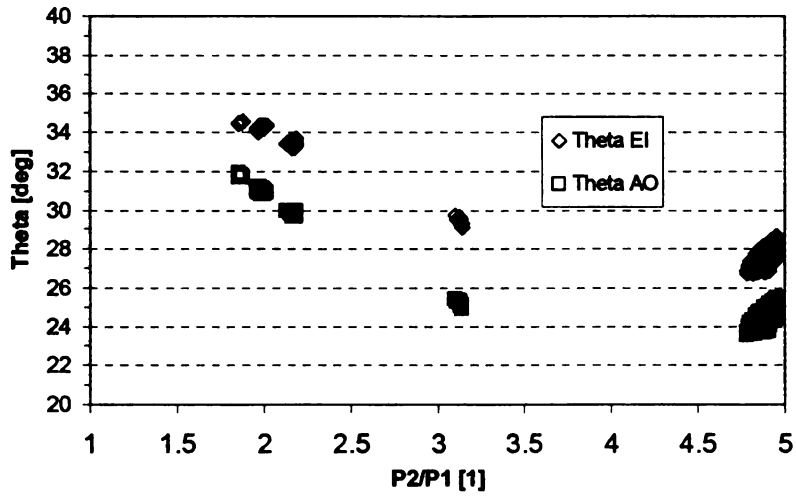

Fig. 40 Change of width of high pressure ports with high pressure gain

Fig. 41 and Fig. 42 deal with the variation of the port widths of the low pressure ports with respect to rotor speed and compression gain.

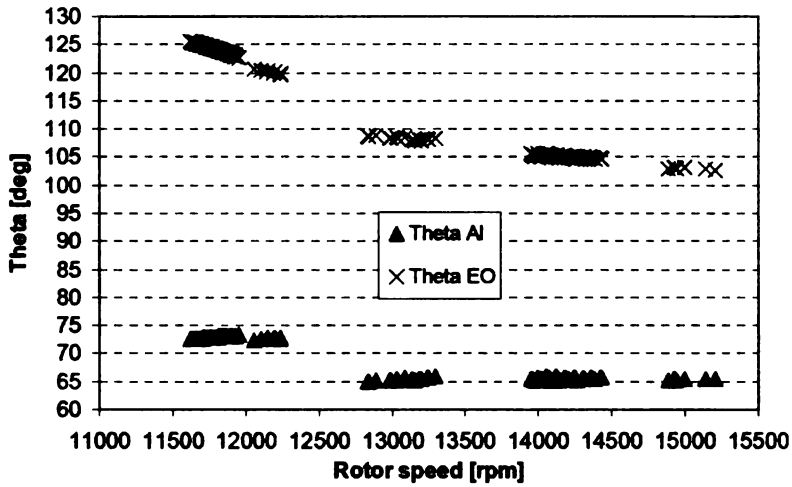

Fig. 41 Change of width of low pressure ports with design speed

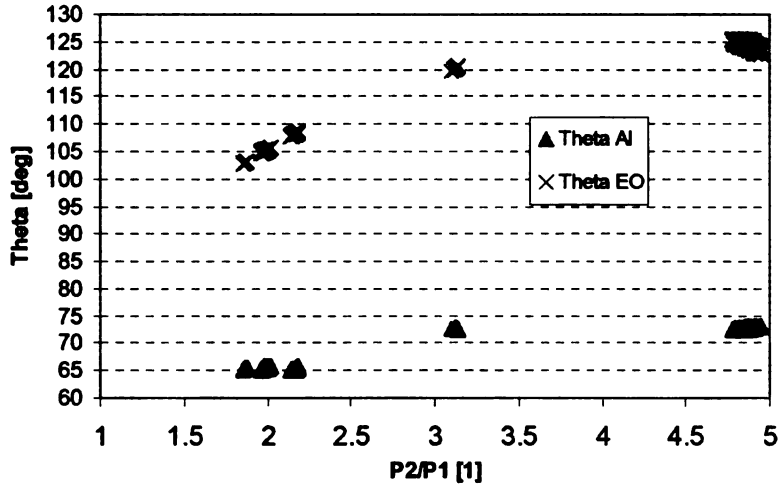

Fig. 42 Change of width of low pressure ports with high pressure gain

5.2.2 **Position of Ports**

This section deals with the variation of the position of the ports with respect to the rotor speed and the compression gain.

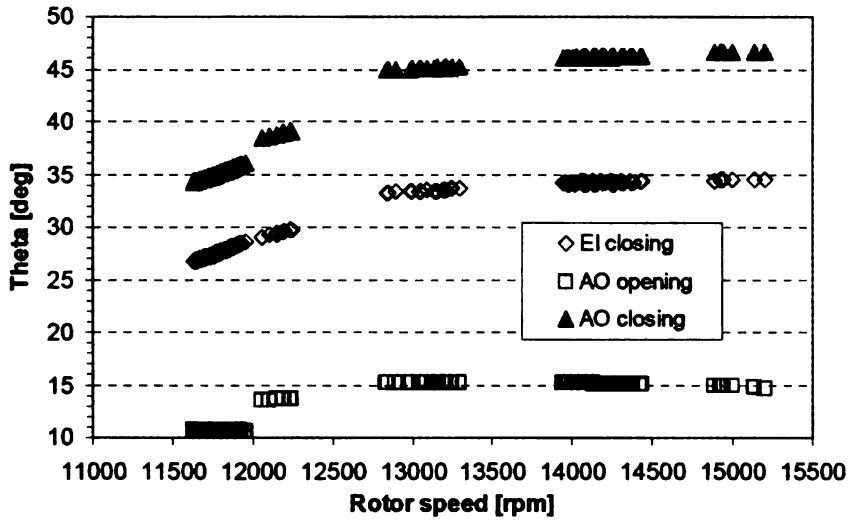

Fig. 43 Change of high pressure ports position with design speed

Fig. 43 presents the trend of port width for the HP region with rotor speed. EI opens at 0° and the width increases with increase in speed. A similar trend can be seen for the AO port width. The opening time has to increase as the rotor travels a greater sector angle at higher speeds.

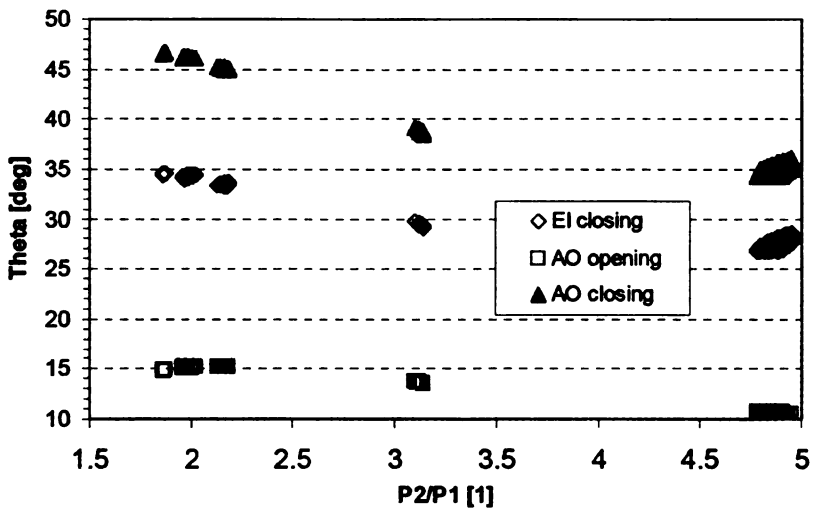

Fig. 44 Change of high pressure ports position with high pressure gain

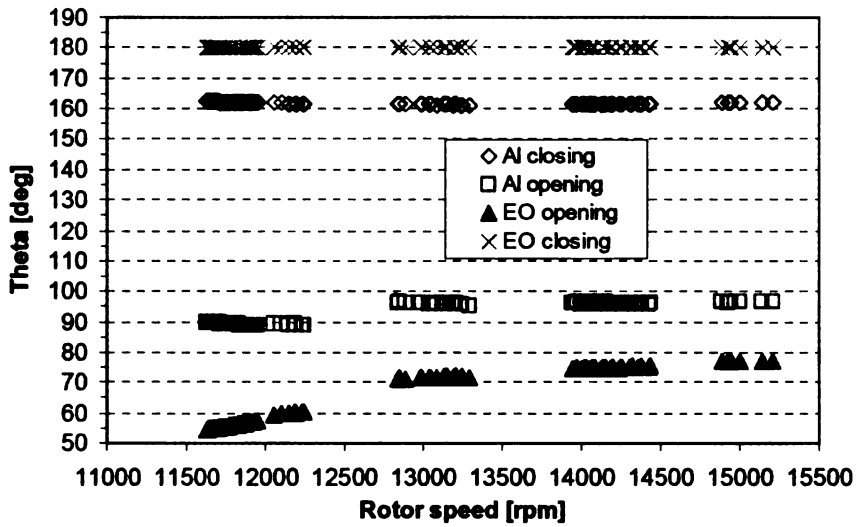

Fig. 45 Change of low pressure ports position with design speed

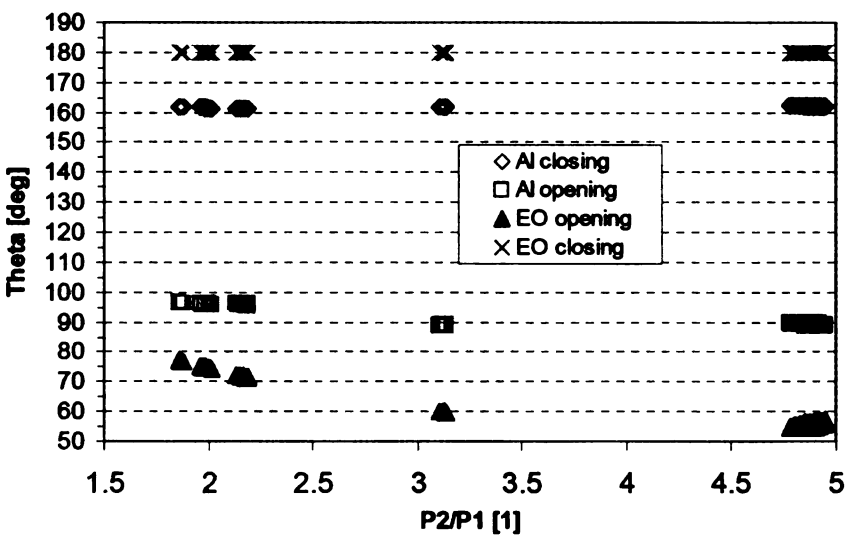

Fig. 46 Change of low pressure ports position with high pressure gain

Fig. 45 and Fig. 46 show how the variation of rotor speed and compression gain affect the position of the ports.

We can see the reduction in size of the EO port width with increasing speed and a similar trend for the AI port. It can be seen that the EO width changes by almost 30° over the

operation range while the AI port changes by less than 10°. This makes the EO port the critical dimension for maintaining the operation condition.

5.3 WAVE PATTERN COMPARISON

Operation Point 2 [20] was chosen to validate the code because of the presence of EGR. It was important to observe if the code would be able to represent this exhaust leakage.

P1	0.99 bar
P2	1.88 bar
P3	1.50 bar
P4	1.01 bar
T1	300 Kelvin
T3	1100 Kelvin

Table 6 Operation Point 2

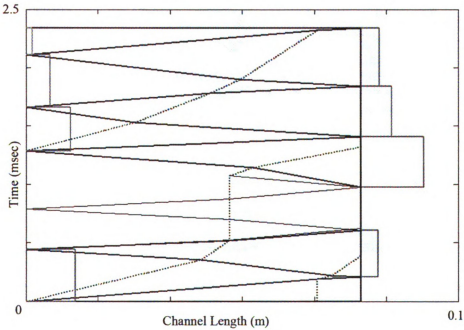

Fig. 47 Output plot of code for Operation Point 2 [20]

Fig. 48 shows the static pressure contour plot of the fluid present inside the wave rotor channels. The wave interactions have been sketched as a reference and it can be seen that they match the assumed wave pattern very well.

The 1D Algebraic code assumes a constant pressure in each zone because it calculates the end states while the FLUENT simulation shows the variation of the pressure in each zone while validating the output of the code. An area of particular interest is zone *IV*. The code assumes that it would be a zone of constant pressure so it would be expected that zone *IV* would be of a homogeneous color but we see that some wave dynamics are still present even though both sides of the channels are closed.

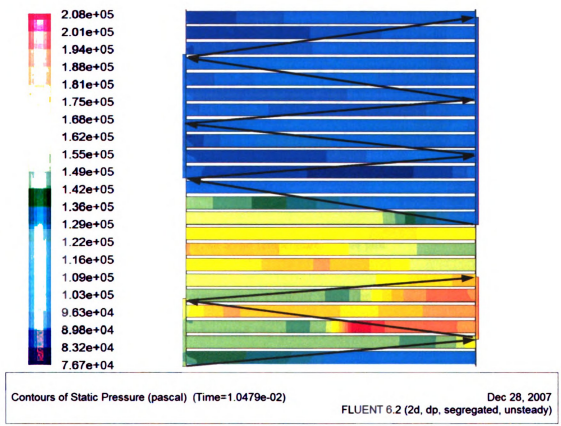

Fig. 48 Static Pressure contour plot with the waves illustrated

Looking closely at zone *IV*, we can see a faint outline of two pressure waves and this result confirms the accuracy of the selection of the two 'virtual' waves in the code.

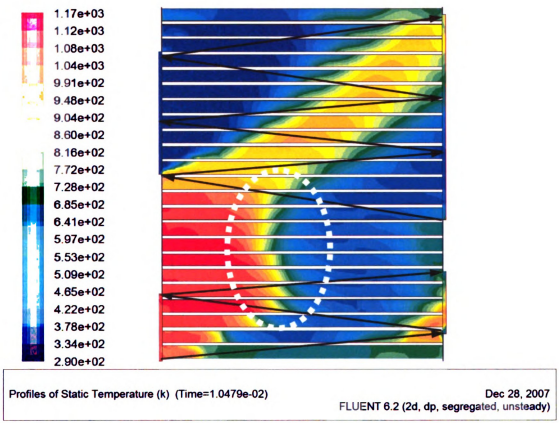

Fig. 49 Static Temperature contour plot

Fig. 49 presents the static temperature contour plot for Operation Point 2 [20]. The temperature plot is used to understand the position of the air-gas interface and also the heat transferred between the two media. The residence time of the fluids influences the heat transfer between them and consequently the mass flow at the ports. Operation Point 2 was chosen for the validation of the code due to the presence of EGR. It was critical to see the influence of EGR on the pressure wave process and to check if the 1D Algebraic

code would be able account for it. As seen from the output plot of the code (Fig. 47), the code can account for EGR to a very close approximation.

An interesting phenomenon noticed was the shift of the air-gas interface in zone *IV* (dotted white line). This can only be visualized in the temperature contour plot while the wave dynamics have to be observed in the pressure contour plot. The ability to plot waves, air-gas interfaces and zone averaged velocities is the biggest advantage of the 1D Algebraic code.

5.4 VELOCITY OUTPUT COMPARISON

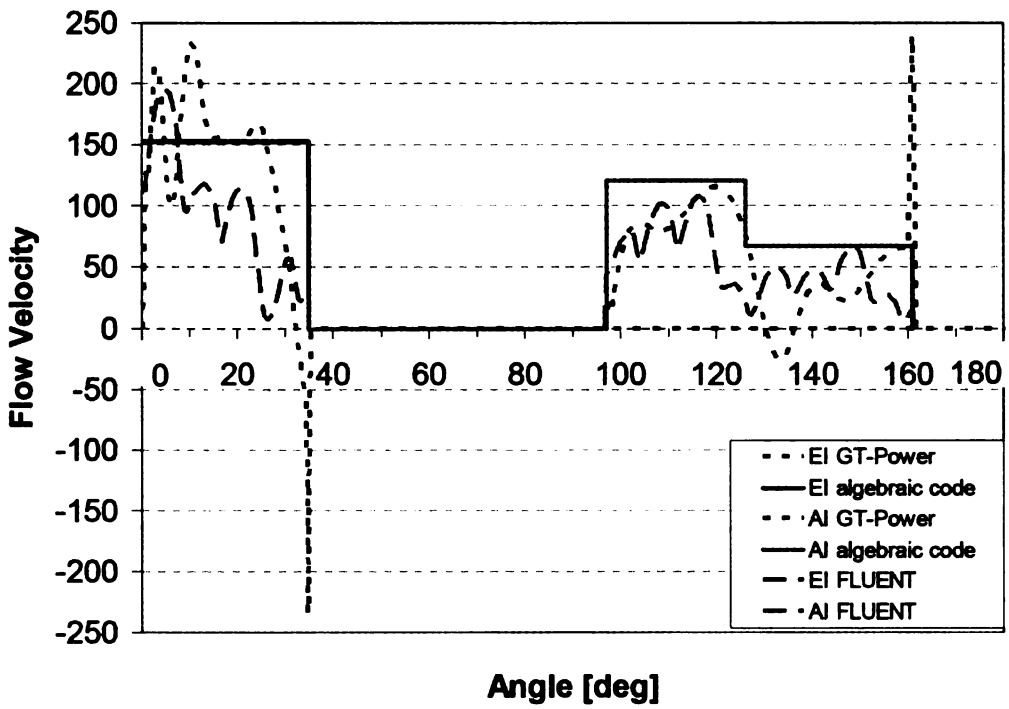

Fig. 50 Comparison of flow velocities at intake side using FLUENT, GT-POWER and the 1D Algebraic code

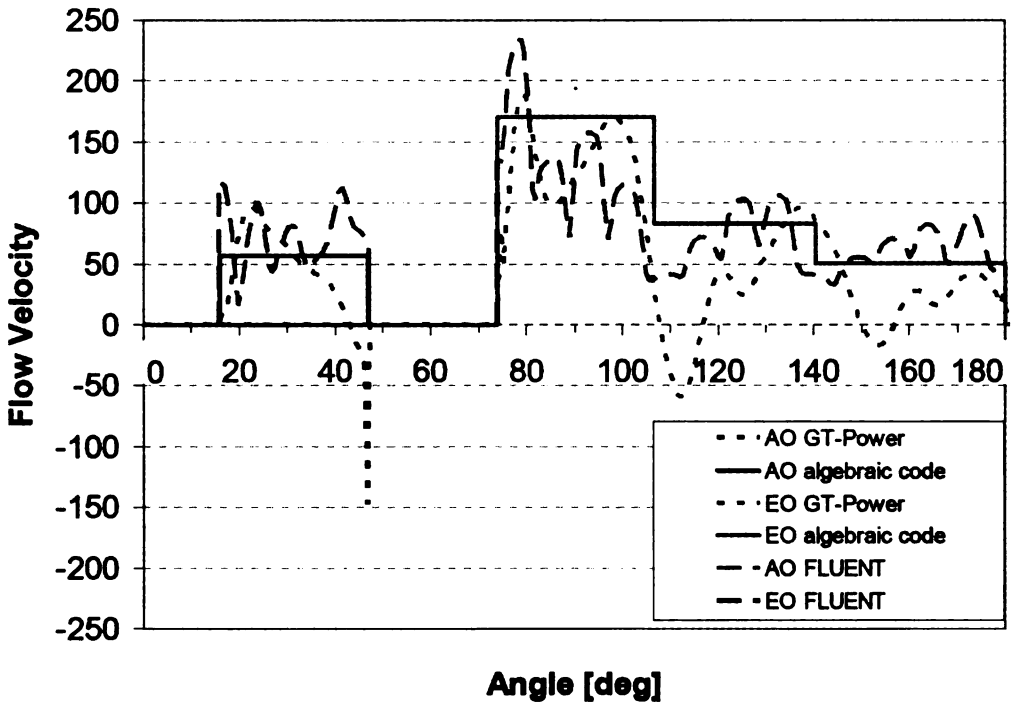

Fig. 51 Comparison of flow velocities at outlet side using FLUENT, GT-POWER and the 1D Algebraic code

From Fig. 50 and Fig. 51 it is clearly visible how well the 1D Algebraic code calculates the flow velocities at the ports. It was expected that the 1D algebraic code would provide port velocities results that would be slightly higher in value as compared to both, FLUENT and GT-POWER models. The reason being both FLUENT and GT-POWER models account for leakage and hence will show lower values of pressure and velocity.

CHAPTER 6

TEST RIG DESIGN

6.1 OPERATION MODES

The gas turbine test rig can have two operation modes, open circuit mode (Fig. 52) or closed circuit mode (Fig. 53). The circuits mentioned here describe the connectivity between the ports which normally are the connections between the high pressure ports (AO to EI) and the low pressure ports (AI to EO).

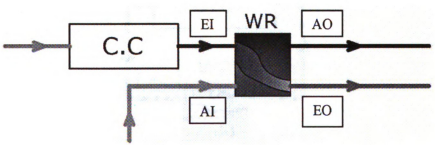

Fig. 52 Open Circuit Mode

For an **open circuit** (Fig. 52), a single stage supercharger is considered. In this system, air is supplied to the combustion chamber (C.C) separately and has no link between the mass flow rates of the EI and AO ports of the wave rotor (WR). This type of circuit is very useful for preliminary design and testing as a variety of flow velocity and pressure conditions can be simulated.

For the **closed circuit** (Fig. 53), a two stage compressor has been considered. The primary stage of the compressor is a turbocharger and the secondary stage of the

compressor is the wave rotor which supplies the air to the combustion chamber. The figure shows the clear link between the mass flows of the high pressure and low pressure region of the wave rotor. The pressure of ambient air is increased by the compressor (C) and supplied to the WR where the high pressure exhaust from the C.C is supplied to the EI port. After the pressure exchange process in the WR, the compressed air is supplied back to the combustion chamber. This closes the loop for the high pressure region.

The EO port supplies to the turbine (T) of the turbocharger and this waste energy is used to pressurize the incoming ambient air at C. Also, a mass balance between the inlet side and the outlet side has to be maintained for such a circuit.

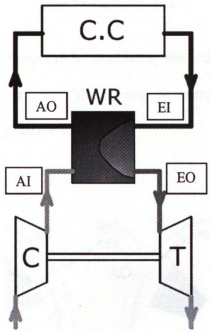

Fig. 53 Closed Circuit Mode

6.2 DESIGN POINT

The 1D algebraic code was run for the validation of the closed circuit mode. Running the code for a large matrix of inputs provided a chance to observe the viable operating

conditions which met the extents that could safely be tested in the laboratory. After analyzing the results and filtering them for the right mass balance requirements, a porting geometry was chosen.

The given operating condition was –

P1	0.96 bar
P2	2.15 bar
P3	1.67 bar
P4	1.00 bar
T1	300 Kelvin
T3	1100 Kelvin

Table 7 Operation Point 3

For this set of pressure and temperature conditions, the code provided an output of the porting geometry and the rotor speed. The porting geometry is given in Fig. 54 and the calculated rotor speed was 12950 (≈ 13000) rpm.

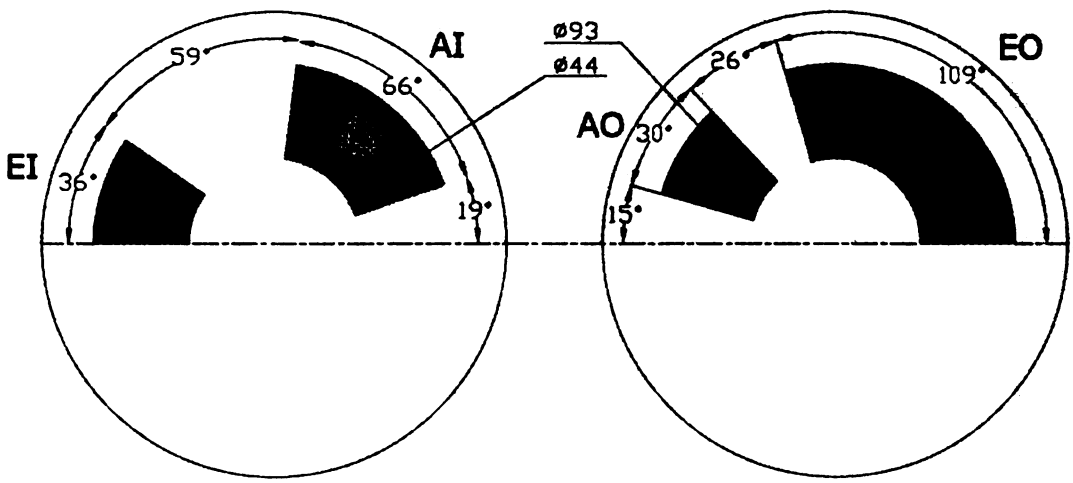

Fig. 54 Porting for given Operation Point 3

6.3 FINITE ELEMENT ANALYSIS

Once the porting geometry and design had been fixed, it was important to analyze the components individually and together at the possible extreme thermal and dynamic conditions.

The wave rotor was analyzed for high rotor velocities due to the chance of it free-spinning (a condition in which the rotor is driven by the momentum of the fluid entering the channels) [19], [29]. Fig. 55 shows the effect of mass flow on the power of the driving motor. Due to the port entry angle and the mass flow rate, beyond a specific speed, the motor behaves like a generator and the rotor becomes self driven. The only forces the rotor has to overcome beyond that are the windage losses between the rotor and casing and the bearing friction. This creates a dangerous condition where the rotor speed is uncontrollable and could lead to the bursting of the rotor and damage to the bearings due to the heat generation or the vibrations.

The displacement of the rotor was also studied for extreme operating conditions and it was found to have a maximum expansion of 0.669mm at 900 Kelvin and 40000 rpm which gave a good factor of safety because the analysis was done by modeling the rotor as steel while the wave rotor is made of a low expansion material.

The wave rotor was found to fail close to 50000 rpm at an operating temperature of 800 Kelvin. The rated speed for the driving motor used in the Turbomachinery Laboratory was 20000 rpm which allowed a large factor of safety (Fig. 56) while being able to accommodate the complete operation range of speeds (as seen previously in the results section).

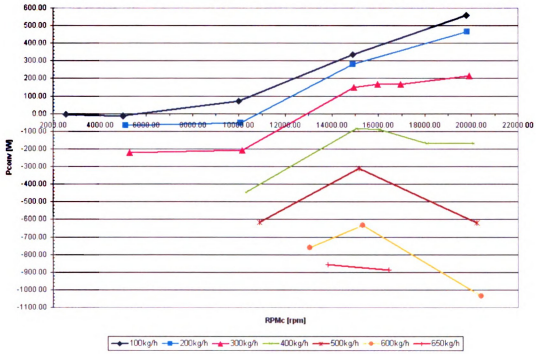

Fig. 55 Mass flow isolines on a graph of Motor Power Vs Rotor RPM [19]

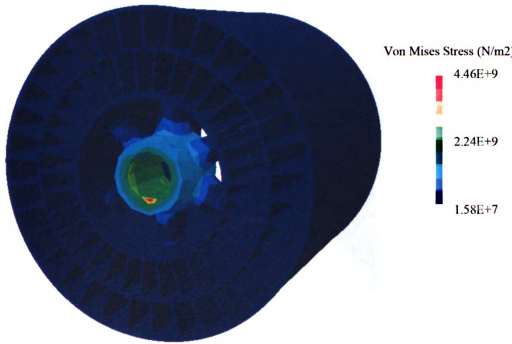

Fig. 56 Stress Analysis of wave rotor at 900 K and 40000 rpm rotational speed

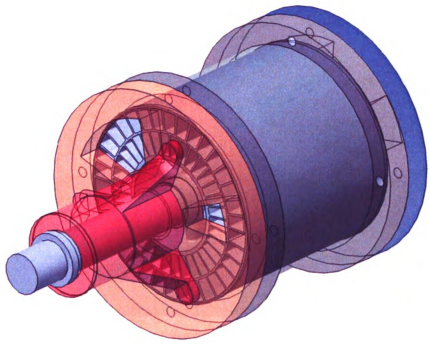

Fig. 57 CAD assembly model of fixed port wave rotor design (without piping)

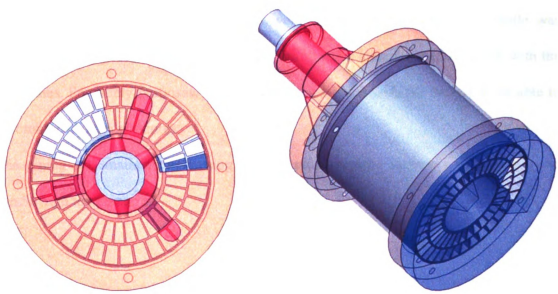

Fig. 58 Top view and oriented view of rig assembly

6.5 CURRENT DESIGN

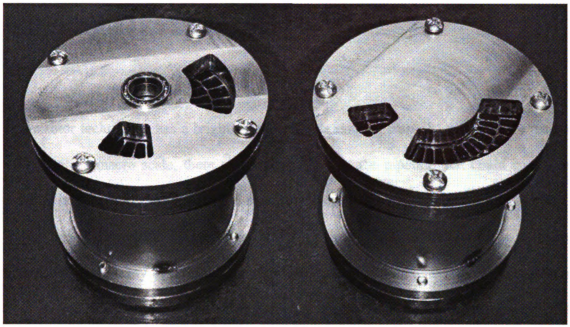

Fig. 59 Photograph of Intake Side end plate (Left) and, Exhaust Side end plate (Right) of current test rig

For the current test rig (Fig. 59), 12 mm thick cast iron discs were used to manufacture the end plates and the appropriate ports were machined into them. The mantle was manufacturer by press fitting a muffler pipe into flanges manufactured to match with the end plates. For safety purposes, the pipe was tack welded with the flanges to be able to accommodate high pressures.

The piping was manufactured using exhaust muffler pipes because of their ability to handle high temperatures.

CHAPTER 7

FUTURE DEVELOPMENTS

Wave rotor technology has a bright future in fields ranging from the micro to the macro scale. On the macro scale, there are developments in the pipeline that could enter the aviation industry with the potential to either enhance or even replace gas turbine engines. In the power generation industry, the wave rotor can be used in a topping cycle to increase the efficiency of power generation devices such as stationary gas turbines. One of the most important applications is with the automotive industry to supercharge internal combustion engines to improve their performance while reducing emissions. Wave rotor technology also finds application in refrigeration units and its feasibility is being investigated.

The micro-scale wave rotor applications are in the field of Unmanned Aerial Vehicles (UAV) and energy producing devices. A concept known as the wave disc engine [25] (effectively a wave rotor with internal combustion) can be used as a propulsion system for UAV's or an even smaller wave disc engine can be coupled with a generator that can replace batteries and run days on a single drop of fuel.

Some of the future wave rotor technologies studied during the course of this research were the **Variable Porting Geometry Wave Rotor** and the **Turbine Wave Rotor**.

7.1 VARIABLE PORTING GEOMETRY WAVE ROTOR

Using the data gathered by running the 1-D code, the variation of the porting geometry with respect to pressure boundary conditions was found. Studying the port variation gives an estimate of the impact that the variation of the porting geometry at any port can have on the performance. The application of a variable porting geometry would give the opportunity to extend the operating range of the wave rotor and help achieve the required efficiency goals. The designs for the Variable Porting Geometry Wave Rotor went through three generations.

1st GENERATION

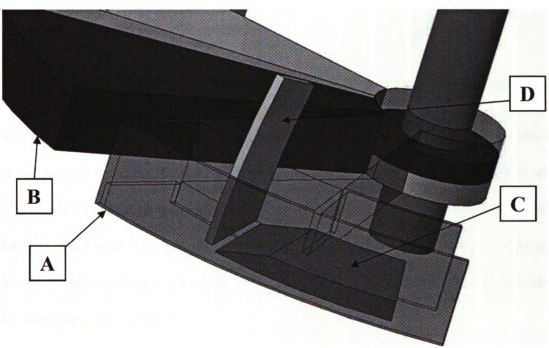

Fig. 60 View of EI port and spacer

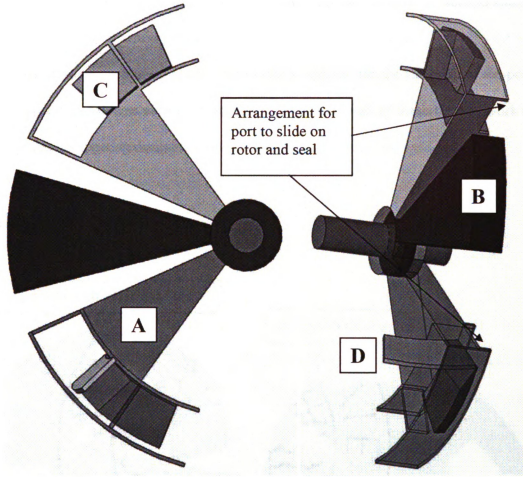

Fig. 61 Top view (Left) and Oriented View (Right) of 1st generation variable porting

The 1st generation of the variable porting wave rotor (Fig. 60 and Fig. 61) rig utilized a set of ports (A) that could 'ride' on the surface of the wave rotor and had a set of shoes (C) which varied the port areas (and/or angles). A flow guiding vane (C) was placed at the end of the shoes to allow the variation of the incidence angle for the flow. The ports would be separated by a spacer (B) which would maintain the distance and the sealing between the ports and the rotor.

This system saw immediate drawbacks, especially since there would have to be a wide range of spacer plates to accommodate different operating conditions. There were too

many surfaces to seal and the guide vane structure was too small to be accommodated successfully at those operating temperatures.

There was no robust actuation system that could be applied for the variation of the ports and nor was it possible to vary the porting actively. Due to all of these factors, work on the 1st generation porting design was discontinued.

2nd GENERATION

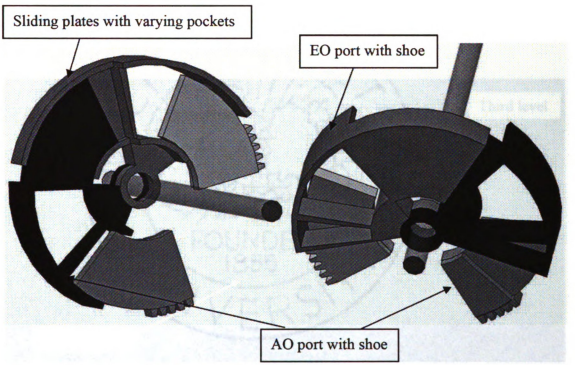

Fig. 62 Second Generation End Plate Structure

The 2nd generation design (Fig. 62) aimed at eliminating the spacer plate of the 1st generation design so that a variable position could be achieved actively. It also added a variable pocket to the structure which has the ability to increase the operating range of the device while slightly lowering the peak performance because of the leakage generated

by the pockets. It was also noticed that the variable gas pockets were present but not variable according to a tuning requirement and would just create an additional leakage space for higher speeds.

Though the total number of sealing faces were reduced, the structure was very complicated and a large restriction would be placed on the porting angle variation. Due to these reasons, a new design had to be implemented.

The 2nd generation assembly design can be seen in appendix B.5 (Fig. 77).

3rd GENERATION

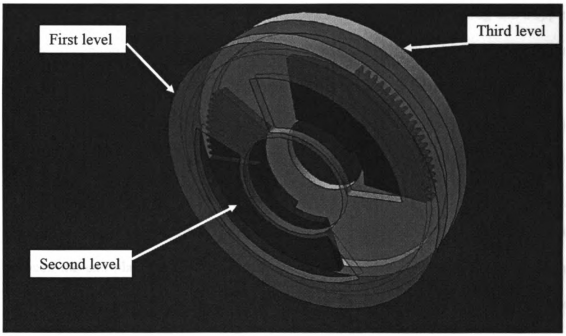

Fig. 63 3 Level Porting Design

The 3rd generation design eliminated the problems of the first two generations by incorporating all the benefits while reducing the leakage spaces from the 1st generation

and eliminating the restriction on the porting variation. The 3rd generation involves a three level porting design (Fig. 63). This adds to structural rigidity though it adds to the total weight of the system.

The first level (transparent disc) is placed as close to the wave rotor channels as possible to reduce the leakage. It is a solid plate with slots cut for the ports.

The second level is composed of the sliding shoes (shown in purple) which vary the porting area and position. These could either be a set of 2 or 4 shoes depending on the needs of the application. 4 shoes can vary both leading and lagging edges of the ports while 2 can only handle one of the two edges. These shoes can be controlled by a stepper motor which is set on the third level of the porting.

The third level of the porting is a support structure for the end plate, piping and stepper motors. The piping can be varied on this level without affecting the other two levels structurally. The motors for varying the port angle and position are mounted on this level which also aids in keeping their temperature lower. The motors can be mounted axially with spur gears or mounted radially with worm gears. The radial configuration is preferred because of the space limitation on piping.

Another improvement in the 3rd generation design was its ability to vary the angle between the end plates as well. One end porting assembly would be mounted in a way that it can be rotated relative to the other which simplifies the porting variation for increased speeds. The offset angle between the two ports is proportional to the rotor speed and this helps reduce the demands on the variation of each edge of the porting making this design extremely desirable.

A test rig assembly layout of the 3rd generation porting design can be seen in Fig. 78.

7.2 TURBINE WAVE ROTOR

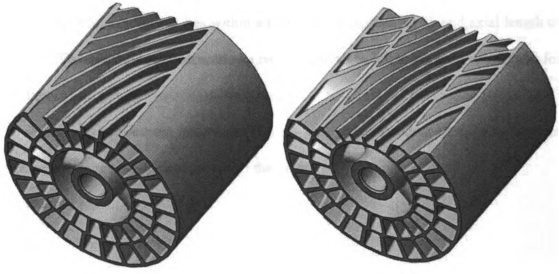

Fig. 64 Cut section of the Turbine Wave Rotor (left) first flute of rotor (right) first and second flute of rotor

In the foreseeable future, a new kind of wave rotor has been proposed which will be able to exceed the duties of the previous channeled rotor drums. The difference between the traditional axial drum (Fig. 10) and the turbine wave rotor lies in the channel geometry. The turbine wave rotor utilizes curved channels to extract shaft work from the momentum of the incoming flow.

This way, the turbine wave rotor has the ability to provide a dual benefit. The first being the similar energy exchange process as the traditional wave rotor but utilizing the momentum of the fluids to either rotate or to provide shaft work. A critical factor in this design is the blade profile design and its optimization. The basic underlying principle of the design is to maximize the momentum transfer from the fluid to the channel walls while maintaining the efficiency of the energy exchange.

PRELIMINARY DESIGN PROCEDURE

Using turbomachinery principles for turbine blade design, a curvature distribution is plotted (Fig. 65). The profile lies within a rectangle of channel width and axial length of the rotor. The design is not restricted to a rectangular space but is assumed rectangular for simplicity.

The dimensions of the axial length and channel width are dependent on the total number of channels required and the diameter of the drum.

$$n \times w = \pi D$$

Where,

n number of channels

w width of channels

D diameter of drum

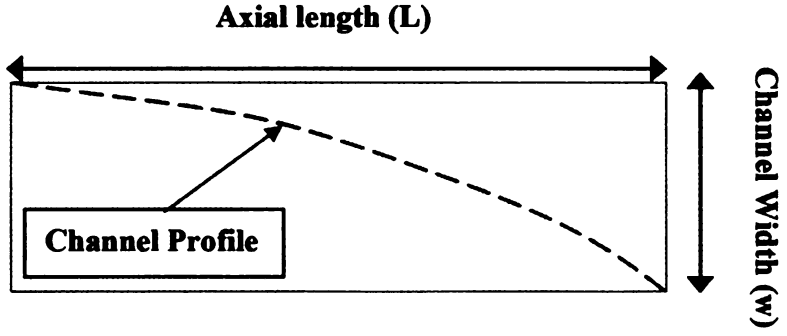

Fig. 65 Diagram of Single Channel

After the values are selected, the developed view (Fig. 66) of the rotor is sized. It can either be wrapped around a drum of the appropriate diameter or a CAD model can be generated using the developed profiles.

A drawback of this procedure is that it cannot account for the three dimensional effects of the flow and assumes a one dimensionality of the flow. This can be either achieved by increasing the number of channels and increasing the number of flutes to achieve a one dimensional flow or can be offset by accurate 3D blade design.

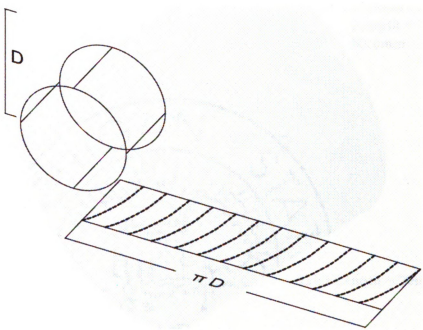

Fig. 66 Developed view of Wave Rotor

The advantages of using such a design are –

- Extraction of work from the gas and air traveling through the channels which will assist the turbine rotor in shaft torque
- Reduction in length of the wave rotor for the same effective length (Fig. 67)
- Reduction in weight and hence moment of inertia of the wave rotor
- Possibility of replacing the turbine itself

The disadvantages of using this design are –

- The component complexity is high
- The manufacturing costs will be high

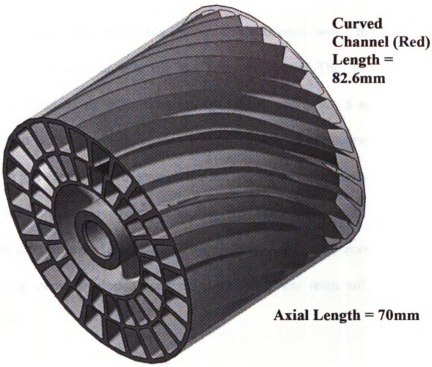

Fig. 67 Comparison of channel and rotor axial length

CHAPTER 8

CONCLUSIONS

From the results accomplished during the course of this research work, the feasibility of a gas turbine topped wave rotor test rig has been validated. The wave rotor shows promising results in achieving higher thermal efficiency and if sized and tuned for the operating condition of the gas turbine, can have a large impact on energy saving. The complexity of the gas exchange process and the required control mechanisms are some of the biggest reasons why the wave rotor technology had been overlooked till now. There is a good chance in the future that the usage of better computation resources and codes such as the 1D algebraic code developed during the course of this work will help bring this technology forward.

The 1D algebraic code developed in this body of research can successfully model the wave phenomenon inside a pressure wave supercharger for a given set of input operating conditions and provide the working speed and individual porting geometry as an output. The simplicity of the code makes it easily customizable and can be altered to run for a variety of pressure wave supercharging techniques some of which are IC engine supercharging and stationary power generation enhancement. The code has also helped aid the preliminary design of the internal combustion wave disc engine [25].

Another tool developed during the course of this research is the parametric characteristic diagram model. This model has helped elucidate the effect of variation of the pressure boundaries and velocities with respect to each other and provides a simple view of the interdependency of the waves propagating in different media. It provides a very good qualitative exposure to the pressure wave phenomenon for both through and reverse flow configurations.

Future developments such as the variable porting design for wave rotors mentioned previously can also be aided by the use of the 1D algebraic code. Due to the speed of computation, an operation state can be computed in a matter of seconds and if hard-coded into a controller or saved as an operation map in the controller, it can actively vary the porting geometry of the test rig with changing pressure and temperature conditions. This will help increase the operational range of the application it has been designed for and provide better performance. The fixed porting design can be incorporated into power generation devices which normally run only at rated speed while the variable porting design can be incorporated into IC engines and turbojet engines which has the potential to increase the fuel efficiency of these devices. The ability of the wave rotor to reduce NOx emissions in IC engine applications has already been studied and quantified [9] which shows an overall benefit to applications when being provided with the ability to reduce emissions, increase efficiency without compromising on performance. All these factors inspire greater confidence in the use of this technology.

APPENDIX A

A.1 SHOCKWAVE PROPAGATION

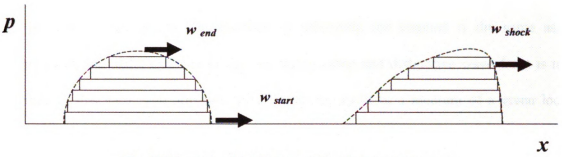

Fig. 68 Schematic of shockwave creation from an overpressure

To understand the propagation of a shockwave, a simple model is defined in Fig. 68. For the generation of any sort of wave, a pressure difference is required which is represented here as an overpressure (dotted line). Assume the overpressure to be composed of a series of small pressure elements (or disturbances). As soon as the first overpressure element starts traveling inside the channel at a particular velocity w_{start}, it increases the pressure and consequently the temperature of the fluid behind it. This leads to an increase in the speed of the wave because the local speed of sound is proportional to the square root of the fluid temperature as shown in equation (2). If the rise of temperature is rapid enough, the entire wave begins traveling as a sharp wave front with the same speed. This is known as a shockwave as the pressure rise is very rapid in the medium.

Shockwaves require high pressure ratios and temperatures for their propagation [16]. The higher the pressure difference, the better the chance of a shockwave being formed. A wave caused by a low pressure ratio is known as a pressure wave.

A.2 PRESSURE WAVES & EXPANSION WAVES

In pressure waves, as the phenomenon of traversing the channel is the same as a shockwave, the difference lies in the fact that a sharp and distinctive wave front is not formed in this case. The pressure wave begins its travel in a medium of a given local speed of sound and ends at a higher speed which is the sum of the local speed and the induced flow velocity. This is the reason why a pressure wave 'spreads' (into components of head and tail waves). The reason why a shockwave does not spread is because the entire sharp wave front is traveling at the same speed (which means the head and tail waves are traveling at the same speed).

As shockwaves and pressure waves are overpressure conditions, we will now consider the underpressure condition for expansion waves.

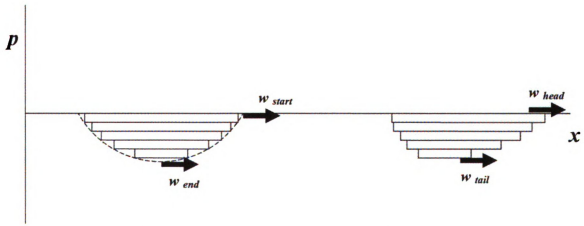

Fig. 69 Schematic of an expansion wave being created by an underpressure

As a negative pressure or underpressure wave begins to propagate in a channel (Fig. 69), we can assume that the front of the wave is called the head and the trough is called the tail. An interesting feature of an expansion wave is that it cannot generate a shockwave.

The velocity of the wave induced by the first pressure element is w_{head} and because of the next pressure element reducing the pressure and temperature of the medium, the velocity of the wave reduces. As the trough is traveling at a reduced velocity w_{tail}, the wave spreads. This is what is known as the 'Expansion Fan'.

A more detailed explanation of the wave phenomenon can be found in ref. [24].

APPENDIX B

(DIAGRAMS)

B.1 GT-POWER MODEL

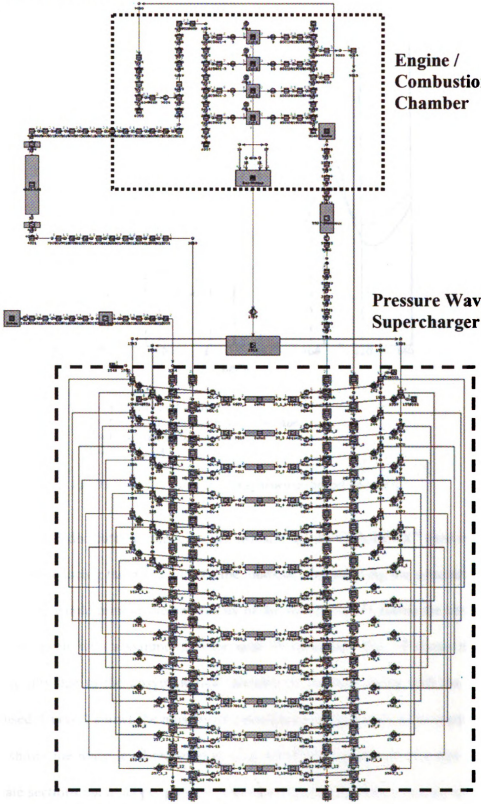

Fig. 70 GT-POWER Layout of Reverse Flow configuration [19]

B.2 NOISE REDUCTION ANALYSIS

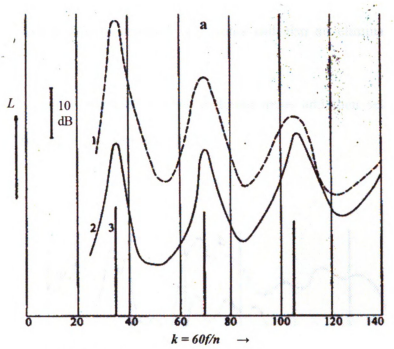

L = Noise level
a : 35 symmetrical divisions
1 = Measured at pressure wave machine
2 = Measured at disc
3 = Calculated

Fig. 71 Noise Level estimate for symmetric channel rotor [27]

Research at ABB dedicated to reducing the 'whistle' of the COMPREX® tried out many techniques for reducing the noise. One of the methods was breaking the symmetry of the channels which would remove the periodicity of the sound. Fig. 71 shows the comparison of the noise levels with a symmetric rotor with 35 channels. Fig. 72 shows the noise analysis results due to the unsymmetrical division of channels along with the division scheme used. Curve 1 shows the noise level calculated at the pressure wave supercharger, Curve 2 shows the noise level recorded at a rig which was composed of a disc with the appropriate sections cut at its periphery to simulate the rotor channel geometry and a high

pressure blast of air was passed through the gaps. Curve 3 represents the calculated resonant orders for the system. It can be seen that they are in close agreement and that the unsymmetrical system shows reduced amplitudes and also an elimination of resonant peaks.

This is done by using channels of three different areas and then setting them in an unsymmetrical sequence as given in Fig. 72.

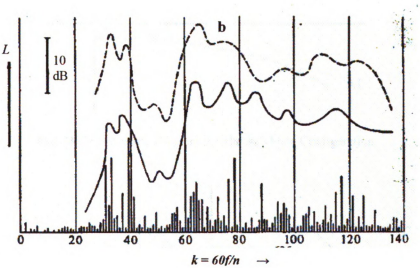

b: 35 unsymmetrical divisions
Division sequence AAA BB CCC B CCC BB AAA B
AAA BB CCC B CC BB AAA B

A = +16.5% , B = -3.5% , C = -15%

Fig. 72 Noise Level estimate for unsymmetric channel rotor [27]

B.3 CHARACTERISTIC DIAGRAMS

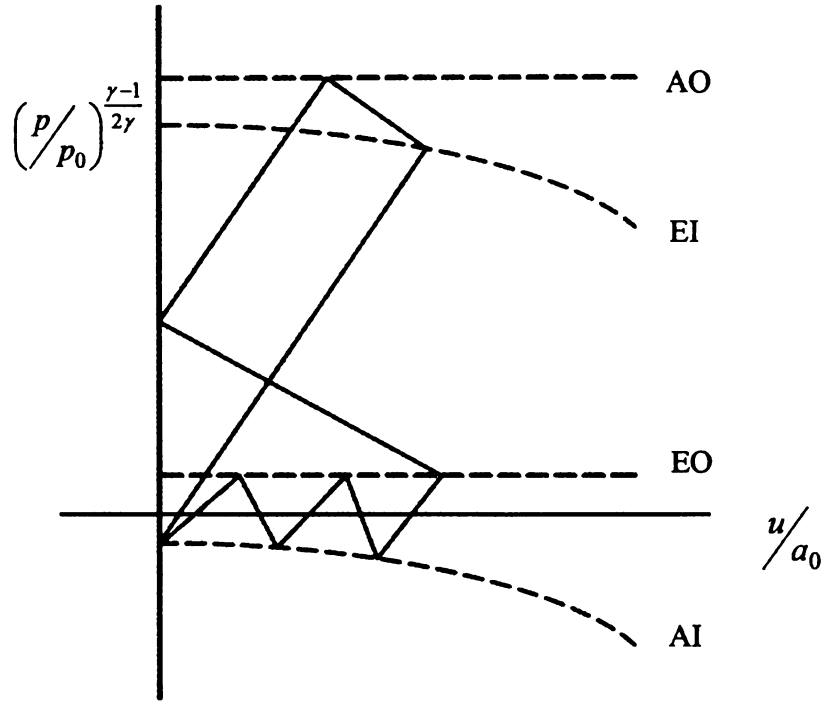

Fig. 73 Characteristic Diagram for Through Flow Configuration

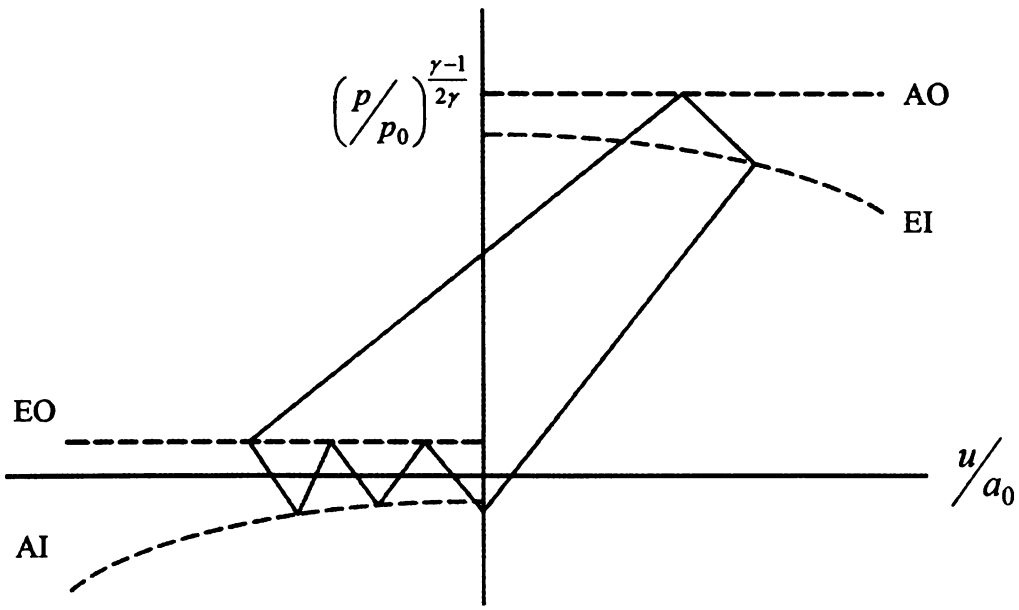

Fig. 74 Characteristic Diagram for Reverse Flow Configuration

B.4 3D PLOTS FROM ALGEBRAIC CODE

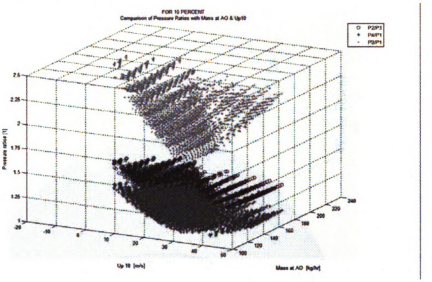

Fig. 75 Plot of Mass flow at AO *Vs* Pressure Ratios *Vs* Zone *X* flow velocity

As the number of parameters for optimization from the output of the code were very high, three dimensional plots were produced to study the dependencies and understand the trends. Fig. 75 illustrates the necessity for 3D plots due to the variation of mass flow rates versus pressure ratio and zone *X* fluid flow velocity. Fig. 76 shows the trend for porting angles with respect to rotor speed and compression gain.

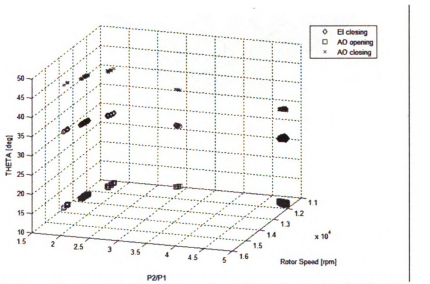

Fig. 76 Plot of Compression Gain *Vs* Rotor Speed *Vs* Porting Angles for EI & AO

B.5 TEST RIG ASSEMBLY MODELS

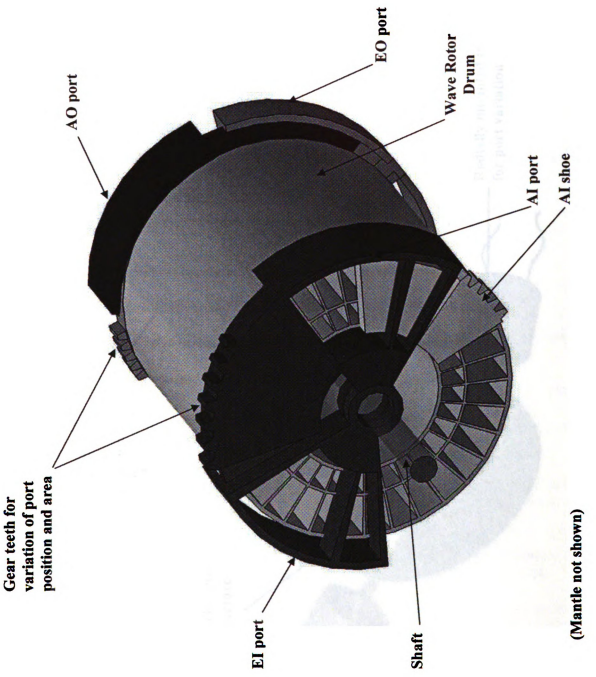

Fig. 77 Assembled 2nd Generation Variable Porting Design

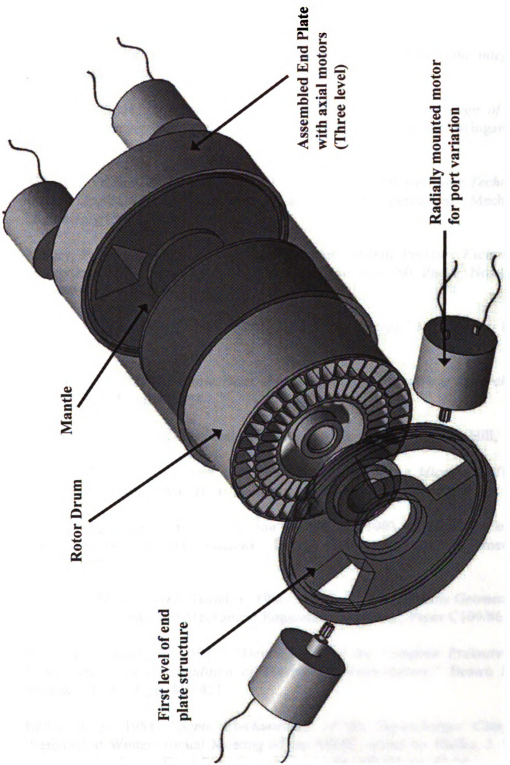

Fig. 78 3rd Generation Variable Porting Test Rig Design

REFERENCES

[1] ABB Project 426 Report, 1994 *"A pressure wave machine with integrated constant volume combustion"*

[2] Akbari, P., 2004, *"Performance Prediction and Preliminary Design of Wave Rotors Enhancing Gas Turbine Cycles"*, Doctoral Dissertation, Michigan State University, Michigan

[3] Akbari, P., Nalim, M.R., and Müller. N., *"A Review of Wave Rotor Technology and its Applications"*, Proceedings of 2004 ASME International Mechanical Engineering Congress & Exposition, 2004

[4] Azoury, P. H., 1965-66, *"An Introduction to the Dynamic Pressure Exchanger,"* Proceedings of the Institution of Mechanical Engineers, 180, Part 1, No. 18, pp. 451-480

[5] Guzzella, L., Martin, R., 1998, *"The SAVE Engine Concept,"* MTZ Report 10, pp. 9-12

[6] Gyarmathy, G., 1983, *"How Does the Comprex Pressure-Wave Supercharger Work?,"* SAE Paper 830234

[7] Heywood, J., *"Internal Combustion Engine Fundamentals"*, McGraw Hill, 1988

[8] Iancu, F., 2005, *"Integration of a Wave Rotor to an Ultra Micro Gas Turbine (UμGT)"*, Doctoral Dissertation, Michigan State University, Michigan

[9] Icingür, Y., Hasimoglu, C., and Salman, M. S., 2003, *"Effect of Comprex Supercharging on Diesel Emissions,"* Energy Conversion and Management, **44**, pp. 1745-1753

[10] Jenny, E., Moser, P., and Hansel, J., 1986, *"Progress with Variable Geometry and Comprex,"* Institution of Mechanical Engineers Conference, Paper C109/86

[11] Jenny, E., Naguib, M., 1987, *"Development of the Comprex Pressure-Wave Supercharger: In the Tradition of Thermal Turbomachinery,"* Brown Boveri Review, 74, No. 8, pp. 416-421

[12] Keller, J. J., 1984, *"Some Fundamentals of the Supercharger Comprex,"* Presented at Winter Annual Meeting of the ASME, edited by Sladky, J. F., Jr., Machinery for Direct Fluid-Fluid Energy Exchange, AD-07, pp. 47-54

[13] Meier, G., Piechna, J., *"Theoretical Analysis of a Working Cycle of the 'Comprex' type Compressor"*

[14] Mayer, A., *"The COMPREX Supercharger – A Simple Machine for a Highly Complex Thermodynamic Process"*

[15] Mayer, A., Oda, J., Kato, K., Haase, W. and Fried, R., 1989, *"Extruded Ceramic - A New Technology for the Comprex® Rotor,"* SAE Paper 890453

[16] Okamoto, K., Nagashima, T., *"Fundamental Wave Process in Narrow Tubes for Micro Wave Rotor Application"*, ASME Paper IMECE 2007-43338, Seattle, Washington, USA, 2007

[17] Pohořelský, L., 2003, *"Auslegung eines Druckwellenladers für einen 1.0l Ottomotor mit 90kW Nennleistung"*, Masters Diploma, Czech Technical Univerity, Prague

[18] Pohořelský, L., Macek,J., Polašek M., and Vítek, O., *"Simulation of a COMPREX® Pressure Exchanger in a 1-D Code"*, SAE Paper 2004-01-1000, SAE International Warrendale 2004, 13 pp.

[19] Pohořelský, L., Obernesser, P., Vavra J., Klir, V., and Macek, J., *"1-D Model and Experimental Tests of Pressure Wave Supercharger,"* ASME Paper IMECE 2007-43427, Seattle, Washington, USA, 2007

[20] Pohořelský, L., Sané, P and Müller. N, *"Wave Rotor Design Procedure for Gas Turbine Enhancement"*, Draft GT-2008-51354, Turbo Expo, Berlin Germany, 2008

[21] Piechna, J., *"Wave Machines, Models and Numerical Simulation,"* Prace Naukowe, Mechanika, z.205, ISSN 0137-2335, Oficyna Wydawnicza Politechniki Warszawskiej, Warszawa 2005

[22] Schruf, G. M., Kollbrunner, T. A., 1984, *"Application and Matching of the Comprex Pressure-Wave Supercharger to Automotive Diesel Engines,"* SAE Paper 840133

[23] Schneider, G., 1986, *"Comprex® Pressure Wave Supercharger in An Opel Senator with 2.3 Liter Diesel Engine,"* Brown Boveri Review, **73**, No. 10, pp. 563-565

[24] Shapiro, A. H., *"The Dynamics and Thermodynamics of Compressible Fluid Flow"*, the Ronald Press Comp., New York 1953

[25] Sharma, K., 2007, *"Preliminary Design Approach to the First Generation Internal Combustion Wave Disc Engine"*, Masters Thesis, Michigan State University, Michigan

[26] Spring, P., 2006, *"Modeling and Control of Pressure-Wave Supercharged Engine Systems"*, Doctoral Dissertation, ETH Zurich, Switzerland

[27] Wunsch, A., 1971, *"Fourier-Analysis Used in the Investigation of Noise Generated by Pressure Wave Machines"* , Brown Boveri Review, No. 4/5/71

[28] Zauner, E., Chyou, Y. P., Walraven, F., and Althaus, R., 1993, *"Gas Turbine Topping Stage Based on Energy Exchangers : Process and Performance"*, ASME Paper 93-GT-58

[29] Zehnder, G., Mayer, A. and Mathews, L., 1989, *"The Free Running Comprex®"*, SAE Paper 890452